Simulating shock interaction with a cavity-embedded cylinder/droplet using a real-fluid hybrid scheme at near-critical conditions

Yu Jiao [1,*] Steffen J. Schmidt [1] and Nikolaus A. Adams [1,2]

[1] *Chair of Aerodynamics and Fluid Mechanics, TUM School of Engineering and Design, Technical University of Munich, 85748 Garching bei München, Germany*

[2] *Munich Institute of Integrated Materials, Energy and Process Engineering (MEP), Technical University of Munich, 85748 Garching bei München, Germany*

(Received 12 November 2023; accepted 16 May 2024; published 3 July 2024)

Examining the influence of shock waves on cylinders and droplets at near-critical conditions, especially when accounting for real fluid effects, represents a relatively unexplored frontier. This research gap becomes even more relevant when extending the investigation to three-dimensional scenarios. The underlying evolution mechanisms at these conditions remain elusive, with limited existing literature. In this study, we present a thorough exploration employing two-dimensional and three-dimensional numerical simulations of a droplet with an embedded gas cavity subjected to a normal shock wave at near-critical conditions. Our approach involves modeling the cylinder/droplet and the surrounding gas flow using the compressible multicomponent equations, incorporating real fluid thermodynamic relationships, and implementing a finite-volume-based hybrid numerical framework capable of capturing shocks and interfaces. To establish the reliability of our approach, we validate it against reference data, demonstrating excellent agreement. We also conduct mesh independence studies, both qualitatively and quantitatively. Our analysis is comprehensive, considering the intricacies of shock impingement, the morphological deformation of the cylinder/droplet and cavity, and the development of vortices. We discuss and analyze various phenomena, including the evolution of wave patterns, jet formation, sheet formation, hole appearance, the emergence of petal-shaped structures or lobes, ligament formation, shear-induced entrainment, and internal cavity (bubble) breakup. We compare the results obtained from the cylinder/droplet with a cavity to those from a planar shock wave impacting a pure cylinder/droplet. We provide a holistic view of the two-dimensional cylinder and three-dimensional droplet's evolution before and after the impact of a shock wave, accompanied by quantitative data regarding the positions of characteristic points along the column over time. Our analysis further scrutinizes the geometrical characteristics of the cylinder and the trends in the distribution of baroclinic vorticity at various stages. Our findings reveal that the presence of a gas cavity plays a pivotal role in shaping the shock wave, which, in turn, influences the generation and distribution of baroclinic vorticity. This leads to a transformation in the unstable evolution process of both the cylinder and the droplet. Importantly, shock waves impacting the evolving interfaces of the cylinder/droplet and the internal gas cavity generate baroclinic vorticity, which subsequently affects the transport and distribution of vorticity, thereby influencing the evolution of the cylinder/droplet interface. In the case of three-dimensional droplets, baroclinic vorticity induces complex, intricate three-dimensional structure transformations.

DOI: 10.1103/PhysRevFluids.9.074002

*Contact author: yu.jiao@tum.de

I. INTRODUCTION

The Richtmyer-Meshkov instability (RMI) manifests when an interface separating two fluids of different densities is suddenly subjected to impacting shock waves. This instability undergoes a linear growth phase followed by nonlinear development, culminating in the formation of numerous small-scale vortices near the interface and ultimately leading to a turbulent mixture [1–4]. This intriguing phenomenon has been studied both theoretically by Richtmyer [5] and experimentally by Meshkov [6], with their contributions laying the foundation for our understanding of shock-induced instabilities.

The implications of RMI extend to various fields, including inertial confinement fusion, space rocket engines, and astrophysics. For space rocket engines, the interaction between shock waves and the fuel-oxidizer interface within the combustion chamber plays a pivotal role in enhancing fuel and oxidizer mixing, thereby reducing combustion distances and engine volumes. This, in turn, significantly improves combustion efficiency and propulsion performance. Shock-droplet interactions are particularly relevant in high-speed propulsion systems [7,8], such as liquid-fueled ramjets and scramjets, especially during processes like startup, mixing, and combustion of high-speed liquid diesel injection. When a high-speed diesel jet enters a combustion chamber where the pressure is near the critical pressure of the fuel droplet, it can induce shock waves that interact with the fuel spray. Hence, exploring RMI and shock-droplet interactions offers valuable insights for optimizing fuel mixing in propulsion systems.

In cases near the critical point, it is essential to consider "transcritical" characteristics, where the combustion chamber pressure approaches the critical pressure of the fuel fluids. Under such conditions, higher temperatures can induce a transition from a liquidlike state to a gaslike behavior, leading to a two-phase mixture [9,10]. For instance, the critical properties of *n*-dodecane are defined by a critical pressure (p_c) of 1.82 MPa and a critical temperature (T_c) of 658.1 K. If *n*-dodecane fuel is injected into a combustion chamber at supercritical pressure ($p/p_c > 1$) and at a temperature below the critical temperature ($T/T_c < 1$), it mixes with hot ambient air or nitrogen, and the temperature of the fuel increases. This can cause the fuel to cross the Nishikawa-Widom line, transforming from a liquidlike fluid to a gaslike supercritical fluid. This unique scenario [11–13], known as "pseudo-boiling," occurs at higher supercritical temperatures and pressures, where fuel fluids exhibit ideal gas behavior when their compressibility factor equals 1.

While many studies have explored near-critical droplets in low-speed convective environments, where droplet evaporation is significantly influenced by viscous effects and heat conduction [14–20], investigations of near-critical droplet interaction with shock waves or high-speed flows are limited. In such high-speed flows, the impact of viscous diffusion, thermal diffusion, and surface tension forces is expected to be negligible. Obtaining detailed experimental data on multiphase shock-driven instabilities, particularly at high pressures and temperatures, remains a challenge. Therefore, numerical experiments have become essential for studying the interaction between shock waves and fuel droplets at near-critical conditions.

In summary, the study of RMI and shock-droplet interactions at near-critical conditions is of great importance and presents various challenges due to the scarcity of experimental data. By conducting numerical experiments, we aim to fill this knowledge gap and contribute to our understanding of fuel mixing processes in high-pressure, high-speed propulsion systems.

Classical simulations of shock-bubble interactions (SBIs) [21–32] and shock-droplet interactions (SDIs) [33–40] have been extensively documented, primarily focusing on scenarios involving pure droplets or pure bubbles. However, these studies have predominantly explored subcritical and supercritical conditions, with limited investigation into near-critical or transcritical conditions. Fluids near their critical points exhibit distinct physical characteristics that differ significantly from classical liquid droplets or ideal-gas bubbles [41–43], necessitating a unique approach.

In SBI-related research, Haas and Sturtevant [21] originally described the intricate phenomena during shock interactions with helium and R22 refrigerant bubbles. Quirk and Karni [22] conducted numerical simulations to characterize SBIs. Bubble compositions of SF_6 and krypton were

subsequently studied [23–31]. However, these investigations were conducted under atmospheric pressure and room-temperature conditions, with the fluids in their gaseous state, classifying them as SBIs.

In SDI-related studies, various processes such as primary shock impingement, droplet deformation, and droplet breakup have been extensively discussed in the literature [5,22,28,44–46]. Duke-Walker *et al.* [47] explored the effects of droplet evaporation and breakup in the context of mixing driven by shock-induced multiphase instabilities. Meng and Colonius [33] investigated the interaction of shock waves with a water droplet, with detailed structures validated against experimental data, including the chaotic flow features in the wake region caused by instability growth. Kaiser *et al.* [48] conducted numerical investigations into water droplet breakup induced by shock impingement and the resulting interface deformation. Sharma *et al.* [49] established a criterion for the transition process between a shear-induced entrainment mode and a Rayleigh-Taylor piercing mode during droplet breakup. Notably, these findings were obtained through both numerical simulations and experimental studies, yet research on near-critical or transcritical conditions [42,43] remains scarce.

Despite existing research, investigations into shock interactions with fuel droplets under near-critical or transcritical conditions remain limited [50–52]. A few studies have explored shock interactions with the *n*-dodecane droplet at near-critical conditions [51] and the shock interaction of a droplet above the critical pressure at varying temperatures around the Widom line [52]. While these studies have provided valuable insights into early droplet breakup behavior and mixing efficiency in high-pressure fuel injection, they have not delved into the detailed simulation of real three-dimensional interface deformation.

Furthermore, the interaction between shock waves and droplets containing gas- or vapor-filled cavities, as well as the interaction between shock waves and bubbles containing droplets, remains a relatively unexplored area within the context of SDIs and SBIs. Previous investigations in this field have primarily focused on scenarios characterized by low temperatures and low pressures [53–59]. In certain industrial contexts, liquid droplets may contain gas cavities, as seen in scenarios involving fuel droplet deformation in scramjet engines or fluid mixing processes [53]. Additionally, there are complexities associated with fluid structures that encapsulate volatile substances, such as perfluoropentane used in ultrasound therapy [54].

A substantial knowledge gap persists regarding the interaction between shock waves and droplets containing embedded gas cavities, particularly under near-critical conditions and in three-dimensional scenarios. Conducting experiments under these demanding conditions is challenging, necessitating robust numerical methods capable of handling intricate flow characteristics. Only a limited number of studies [55–59] have addressed this issue, and those have been conducted at low temperatures and low pressures (at ambient conditions). For example, the interaction of shock waves with droplets containing gas bubbles has been explored under ambient conditions [55], shedding light on the impact of bubble collapse on shock-droplet interactions. Wang *et al.*'s work [56] investigated the shock-accelerated gas ring, providing insights into its evolution and proposing a straightforward method for predicting circulation. Feng *et al.* [57] experimentally delved into the shock interaction with an SF_6 ring, studying the effects of the internal gas cylinder on the evolution of the SF_6 ring with various radius ratios. Liang *et al.* [58] experimentally examined the shock interaction with a water droplet containing an internal vapor cavity. In the numerical realm, Xiang and Wang [59] scrutinized the shock interaction with a water column harboring an internally positioned air cavity.

To the best of our knowledge, the interaction of a shockwave with a droplet embedded with a gas cavity under near-critical conditions has not been investigated in three-dimensional cases. The present study employs numerical simulations to investigate the interaction of a planar shock wave with a diesel cylinder/droplet, both with and without a gas cavity, under near-critical conditions. This research marks the investigation into the effects of an embedded cavity on a droplet under near-critical conditions using a hybrid scheme with a real fluid model. It takes into consideration the three-dimensional nature of the droplet, providing valuable insights for practical applications.

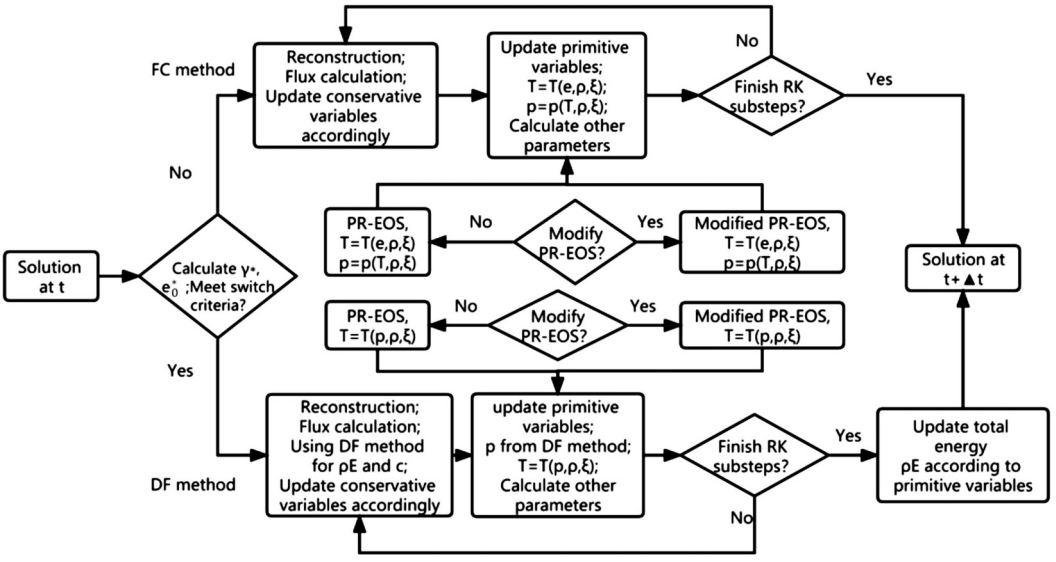

(a)

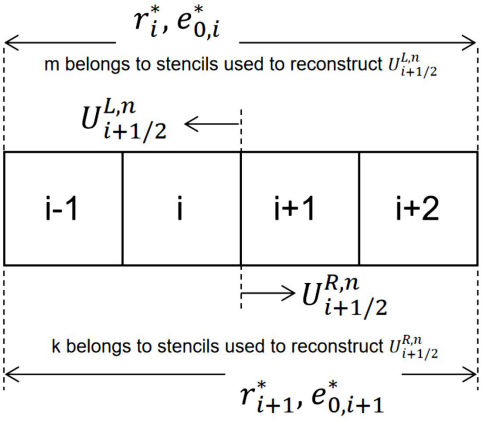

(b)

FIG. 1. (a) Flowchart of the current numerical scheme: fully conservative scheme with PR-EOS/modified PR-EOS and quasiconservative scheme (double-flux method) with PR-EOS/modified PR-EOS. (b) Schematic diagram of the double flux model with the fluxes at the cell face $i + 1/2$.

II. METHODOLOGY

A. Hybrid numerical model

In our study, we employ a hybrid numerical model that can seamlessly transition between a fully conservative (FC) scheme and a quasiconservative (QC) scheme under specific conditions. This hybrid approach significantly reduces pressure oscillations [41] and minimizes energy conservation losses [51] when a shock wave interacts with the interface, e.g., between nitrogen and *n*-dodecane.

The QC scheme employs either a pressure evolution (PE) equation [60–65] or the double-flux (DF) [11,66] method. In this particular study, we utilize the DF method. Figure 1(a) provides a flowchart of the model. We will elaborate on the specific details of this model in the subsequent sections. PR-EOS denotes Peng-Robinson equation of state.

The time integration is performed by an explicit, second-order-accurate low-storage four-step Runge-Kutta method with an enhanced stability region. A detailed description can be found in Refs. [67,68]. The Courant-Friedrichs-Lewy (CFL) value is generally set to 0.5 unless otherwise stated.

1. Fully conservative scheme with PR-EOS

In this section, we describe our fully conservative scheme with the Peng-Robinson equation of state (PR-EOS) for modeling the behavior of the liquid and gas components in our system.

We have extended and enhanced an existing fully compressible one-fluid model, which is an integral part of our proprietary solver, CATUM [67–70]. This model is based on the compressible Euler equations, where the vector of conserved quantities $\mathbf{q} = (\rho, \rho\mathbf{U}, \rho E, \rho\xi_i)$ is computed from $\partial \boldsymbol{q}/\partial t + \nabla \cdot \boldsymbol{F}_i(\boldsymbol{q}) = 0$. Here, ρ is the density, $\boldsymbol{F}_i(\boldsymbol{q})$ is the flux vector, $\mathbf{U}$ is the velocity vector, $\rho E = \rho(e + |\boldsymbol{U}|^2/2)$ is the total energy and e is the internal energy, and ξ_i refers to the mass fraction of component i and for in-total mass fraction of l species $\sum_{i=1}^{l} \xi_i = 1$. For two species, $\xi_1 + \xi_2 = 1$.

In our mathematical model, we neglect several factors, including gravity, heat transfer (thermal conduction), viscous effects, surface tension, and chemical reactions. These omissions are justified due to the extremely short interface interaction time in shock-droplet interaction. Gravity, heat transfer, and viscous effects may become relevant in longer-duration interactions or low-speed scenarios. Surface tension can be disregarded in transcritical flows [10,71–76] because the surface tension coefficient decreases significantly near the critical point. To simplify representation, we refer to the contiguous fuel region as "droplet."

We employ the PR-EOS [77] for both liquid and gas components, as expressed in Eq. (1):

$$p = \frac{RT}{v - b} - \frac{a}{v^2 + 2bv - b^2}, \tag{1}$$

where T is the temperature, R is the universal gas constant, V is the molar volume, $V = M/\rho$, M is the molar mass, and a and b are coefficients. Detailed information on the parameters for the NASA polynomials [78] used to calculate internal energy, enthalpy, and entropy can be found in Appendix A.

In the fully conservative scheme, temperature is updated first, considering internal energy, density, and species mass fractions. This is accomplished using a gradient descent or Newton method. Notably, we can improve the convergence speed of the gradient descent or Newton method for temperature calculation by utilizing the temperature from the previous time step as an initial guess.

2. Quasiconservative scheme with PR-EOS

In this section, we discuss the quasiconservative scheme utilizing the PR-EOS and the DF method [11,66,79] to model near-critical flows. Quasiconservative schemes, such as the DF method, have been developed in recent years and are well suited for addressing the challenges posed by near-critical flow scenarios.

The DF method [11,66,79] was initially proposed by Abgrall and Karni [66] for multicomponent ideal-gas flows and later extended by Billet and Abgrall [79] for ideal-gas reacting flow systems. Subsequently, high-order schemes based on the DF method have been developed [11,80,81]. In our work, we integrate the double-flux-based model of Ma *et al.* [11,82] to handle the current near-critical flows. It is worth noting that the numerical analysis, processing, and discussion are applicable to both the PE [62,83] and DF methods. These two methods exhibit similar performance and conservation behavior in transcritical flows and are comparable to each other in handling contact interface problems [82].

The double-flux model is employed when specific parameters that exceed certain recommended values, as defined in Eqs. (2) and (3), are met:

$$\Delta\Gamma^*_{i,\max} = \max(|\Gamma^*_{i+1} - \Gamma^*_i|, |\Gamma^*_i - \Gamma^*_{i-1}|), \tag{2}$$

$$\Delta e^*_{0,i,\max} = \max(|e^*_{0,i+1} - e^*_{0,i}|, |e^*_{0,i} - e^*_{0,i-1}|), \tag{3}$$

In Ref. [51], it is recommended that $\Delta\Gamma^*_{i,\max} = 1$, $\Delta e^*_{0,i,\max} = 1000$ kJ/kg. Under these conditions, the fully conservative numerical scheme transitions to a quasiconservative scheme based on the criteria mentioned earlier. Another parameter, $|\nabla\rho|/\rho = 0.3$, could also be employed for this purpose [50]. It should be noted that this parameter $|\nabla\rho|/\rho$ is not adopted, but is provided as an option.

The primary characteristic of the DF model [11,51,66,79] is that it maintains the effective specific heat ratio (γ^*) and effective reference internal energy (e^*_0) as constant values in both space and time to mitigate spurious pressure oscillations and oscillations of other physical parameters that may result from pressure fluctuations. Essentially, the relationship between pressure and internal energy remains fixed in both space and time, effectively transforming the local system into a calorically perfect gas system.

The parameters $\gamma^*(\Gamma^*)$ and e^*_0 are determined based on the values from the previous time step to establish relations between internal energy and pressure [82]. This approach [11,66] is taken to prevent abrupt changes in $\gamma^*(\Gamma^*)$ and e^*_0 between cells, as such variations could disrupt pressure equilibrium and induce spurious pressure oscillations. In this process, the effective specific heat ratio (γ^*) is calculated as $\gamma^* = \rho c^2/p$, the effective reference internal energy (e^*_0) is obtained as $e^*_0 = e - \Gamma^* p/\rho$, and Γ^* is calculated as $\Gamma^* = 1/(\gamma^* - 1)$. These values are held constant throughout all Runge-Kutta (RK) substeps within each time step to ensure stability and accuracy. A schematic of the double-flux model is shown in Fig. 1(b).

In each time step of our simulation, the following operations are implemented.

Step 1. Reconstruction and flux computation at the cell faces involves using Eqs. (4) and (5) for left and right face reconstructions:

$$c = \sqrt{p\gamma^*/\rho}, \tag{4}$$

$$(\rho E)^* = \rho e^*_0 + \frac{1}{2}\rho|\mathbf{u}|^2 + \Gamma^* p = \rho e^*_0 + \frac{1}{2}\rho|\mathbf{u}|^2 + \frac{p}{\gamma^* - 1}. \tag{5}$$

When reconstructing the total energy of the left-hand side (belonging to $U^{\mathrm{L},n}_{i+1/2}$) of the cell interface $i + 1/2$, the parameters γ^*_i and $e^*_{0,i}$ of the left first cell i and the values p_m, ρ_m, and u_m of cell m are used to update $(\rho E)^*_m$ of cell m (where m is part of the stencils used to reconstruct $U^{\mathrm{L},n}_{i+1/2}$), then the left-hand-side total energy is constructed according to the corresponding scheme:

$$(\rho E)^n_m = \rho^n_m e^{*,n}_{0,i} + \frac{1}{2}\rho^n_m|u^n_m|^2 + \frac{p^n_m}{\gamma^{*,n}_i - 1}. \tag{6}$$

Similarly, when reconstructing the total energy of the right-hand side (belonging to $U^{\mathrm{R},n}_{i+1/2}$) of the cell interface $i + 1/2$, the parameters γ^*_{i+1} and $e^*_{0,i+1}$ of the right first cell $i + 1$ and the values p_k, ρ_k, and u_k of cell k are used to update $(\rho E)^*_k$ of cell k (k belongs to stencils used to reconstruct $U^{\mathrm{R},n}_{i+1/2}$). The total energy of the right-hand side is then constructed accordingly:

$$(\rho E)^n_k = \rho^n_k e^{*,n}_{0,i+1} + \frac{1}{2}\rho^n_k|u^n_k|^2 + \frac{p^n_k}{\gamma^{*,n}_{i+1} - 1}. \tag{7}$$

Step 2. Obtain the conservative variables and the corresponding primitive variables such as velocity, density, and energy.

Step 3. Update other primitive variables such as pressure for each cell using Eq. (8):

$$p = \frac{1}{\Gamma^*}\left(\rho E - \rho e^*_0 - \frac{1}{2}\rho|\mathbf{u}|^2\right) = (\gamma^* - 1)\left(\rho E - \rho e^*_0 - \frac{1}{2}\rho|\mathbf{u}|^2\right). \tag{8}$$

When updating p_i^{n+1} of cell i, the frozen values $\gamma_i^{*,n}$, $e_{0,i}^{*,n}$, and $\Gamma_i^{*,n}$ from the last substep n and the updated $\mathbf{u}_i^{n+1}$, ρ_i^{n+1}, and $(\rho E)_i^{n+1}$ are used,

$$p_i^{n+1} = \frac{1}{\Gamma_i^{*,n}}\left((\rho E)_i^{n+1} - \rho_i^{n+1}\, e_{0,i}^{*,n} - \frac{1}{2}\rho_i^{n+1}\left|u_i^{n+1}\right|^2\right)$$
$$= \left(\gamma_i^{*,n} - 1\right)\left((\rho E)_i^{n+1} - \rho_i^{n+1}\, e_{0,i}^{*,n} - \frac{1}{2}\rho_i^{n+1}\left|u_i^{n+1}\right|^2\right). \tag{9}$$

Step 4. After obtaining the pressure, update the temperature using the equation of state (EOS) based on density, pressure, and species mass fraction.

Step 5. Update other parameters such as speed of sound, enthalpy, and entropy based on the temperature, pressure, density, velocity, total energy, and internal energy obtained.

At the end of all Runge-Kutta substeps within each time step, the total energy is updated. This update is done according to $\rho E = \rho e + 1/2\rho|u|^2$ and thermodynamic relations $\rho E = \rho E(p, \rho, T, Y)$ to ensure thermodynamic consistency since the temperature is updated after the pressure in Eq. (6).

In the QC scheme, pressure is obtained directly from the DF model [Eq. ((8) and is, therefore, more easily maintained as positive. The temperature is then updated according to the pressure, density, and species mass fraction [11]. However, because different values of γ^* and e_0^* are used for each cell, the two energy fluxes at a face are no longer the same, unlike in the FC scheme. This can result in an energy conservation error. Nevertheless, it has been reported [11,66,82] that the total energy conservation error decreases as the resolution increases and the difference in γ^* between neighboring cells decreases.

3. Hybrid numerical model with modified PR-EOS

The hybrid numerical model, incorporating a modified PR-EOS, is introduced to address two primary challenges:

(1) Conservative scheme-induced problem: When using a FC method with the classical PR-EOS, pressure is updated from temperature and density within each time step, involving a complex nonlinear real-fluid EOS. During this process, numerical diffusion and dispersion can result in negative pressure or induce pressure oscillations, which may lead to simulation failures. FC schemes struggle to maintain pressure equilibrium across transcritical contact interfaces. In contrast, QC schemes are more effective in reducing spurious pressure oscillations and achieving positive pressure. Additionally, reducing the high-order numerical scheme to a low-order numerical scheme can help to mitigate pressure oscillations.

(2) Vapor dome problem: The classical PR-EOS is designed for use outside the vapor dome, and it needs to be modified to handle conditions within the vapor dome. In certain situations, negative pressures can occur for specific density values at relatively low temperatures, and the speed of sound may become complex valued in the vapor dome [84]. Inside the vapor dome, the thermodynamic state described by the classical PR-EOS is either metastable, or unstable or nonconvex.

To address the first issue, the QC scheme provides an effective solution. Moreover, by reducing the high-order numerical scheme to a low-order numerical scheme, pressure oscillations can be reduced.

To tackle the second issue, a modified PR-EOS [51] is introduced to approximate the fluid state within the vapor dome region. This modified PR-EOS ensures that the speed of sound remains above 1 m/s, enhancing the robustness of the numerical method when the state falls within the vapor dome. It is important to note that phase separation is not expected [85,86], and the proposed numerical procedure in Ref. [71] is adequate for resolving pressure oscillations in transcritical flows.

This modification to the PR-EOS enhances the accuracy and stability of simulations, particularly in cases where conditions within the vapor dome need to be represented. For more details, please refer to Appendix C.

B. Numerical methods

It is worth noting that, within the references related to transcritical flow [51,52], it has been observed that the WENO3-type scheme outperforms WENO5 in terms of pressure oscillations, particularly in near-critical or transcritical scenarios. Reference [52] specifically recommends the use of the WENO3-type scheme to simulate higher-strength shock-droplet interactions, thus improving numerical stability. In the case of a Mach 2 shock, they even employ a minmod flux limiter based on the gradient of the mass fraction [52]. Reference [51] demonstrates that reducing the order of reconstruction from WENO5 to WENO3 results in a significant reduction in pressure fluctuations, from 8 to 3.2 MPa. This reduction is attributed to the increased numerical diffusion provided by WENO3. It is evident that WENO3 enhances the numerical stability of the solver and the robustness of the numerical scheme. However, it is important to acknowledge that while the compact reconstruction stencils can reduce computational effort, they also yield results of reduced accuracy when compared to the same mesh resolution with WENO5. To overcome this accuracy limitation of WENO3, an increase in mesh resolution and computational resources is required. At this higher resolution, the results can be made comparable to those obtained with WENO5 [51].

In light of these findings, the current study replaces WENO5 [51] with a WENO3-type scheme to enhance the numerical stability in complex cases. This ensures that the current numerical scheme maintains the key characteristics of the reference scheme. It will be meticulously validated to handle the near-critical shock interactions with *n*-dodecane. The results of these validation cases will be presented in detail and compared with the previous results obtained using the WENO5-type scheme, which can be found in Sec. II C and Appendixes D and E.

The following section describes the classic JS-WENO3 and OWENO3 [87] schemes that will be employed in the validation cases. Specifically, a WENO3-type scheme is employed for reconstruction of pressure, density, velocity, internal energy, and mass fraction to achieve numerical consistency. Interface diffusion is controlled by local adjustment of smoothness indicators and ENO stencil weights. Consider the JS-WENO3 reconstruction for mass fraction ξ as an example:

$$\xi_{\text{gas}}\left(x_{\frac{1}{2}}\right) = w_0 \xi_{\text{gas}}^{\text{L}} + w_1 \xi_{\text{gas}}^{\text{R}}. \tag{10}$$

The left- and right-hand-side interpolation polynomials at the cell interface are $\xi_{\text{gas}}^{\text{L}} = -(1/2)f_{-1} + (3/2)f_0$, $\xi_{\text{gas}}^{\text{R}} = (1/2)f_0 + (1/2)f_1$. Smoothness indicators are defined as $I_0 = (f_0 - f_{-1})^2$, $I_1 = (f_1 - f_0)^2$. f_i is the variable embedded in cell i. The nonlinear ENO stencil weights are denoted as $w_0 = \alpha_0/(\alpha_0 + \alpha_1)$ and $w_1 = \alpha_1/(\alpha_0 + \alpha_1)$, where $\alpha_0 = c_0/(I_0 + \varepsilon)$ and $\alpha_1 = c_1/(I_1 + \varepsilon)$, with c_0 and c_1 being 1/3 and 2/3, respectively.

Additionally, an improved WENO3 scheme, OWENO3 [87], is adopted for comparsion, which maintains the advantages of JS-WENO3 with reduced dissipation. For OWENO3, an additional fourth node is included in the calculation of weights (measuring smoothness), based on a WENO approach with unconditional third-order optimal accuracy on smooth data, and without relying on any tuning parameters. The reconstruction domain is kept to a maximum of four points, consistent with classical WENO3 schemes. The corrected OWENO3 stencil weights are defined as follows:

$$w_0 = \tfrac{1}{3}w + (1 - w)\widetilde{w_0}, \quad w_1 = \tfrac{2}{3}w + (1 - w)\widetilde{w_1}, \tag{11}$$

where $\widetilde{w_0} = (I_1 + \varepsilon)/(I_0 + I_1 + 2\varepsilon)$ and $\widetilde{w_1} = (I_0 + \varepsilon)/(I_0 + I_1 + 2\varepsilon) = 1 - \widetilde{w_0}$, with ε being a small value ($\varepsilon = 1 \times 10^{-6}$), and a corrector weight defined as $w = \text{J}/(\text{J} + \tau + \varepsilon)$, where $J = I_0(I_1 + I_2) + (I_0 + I_1)I_2$ and $0 \leqslant w \leqslant 1$. τ represents the product of the square of the undivided difference associated with the extended stencil (four stencils) and the sum of the smoothness indicators, $\tau = dI$, where $d = (-f_{-1} + 3f_0 - 3f_1 + f_2)^2$ and $I = I_0 + I_1 + I_2$. An additional smoothness indicator I_2 using the additional node is employed for smooth indicators, leading to $I_0 = (f_0 - f_{-1})^2$, $I_1 = (f_1 - f_0)^2$, and $I_2 = (f_2 - f_1)^2$.

OWENO3 is a valuable choice for the following reasons:

(1) It achieves unconditionally optimal accuracy when the data are smooth, and provides second-order accuracy when a discontinuity crosses the stencil. The accuracy properties of OWENO3 are

TABLE I. Initial conditions for shock-cylinder interaction at near-critical conditions.

Stage	p (MPa)	u (m/s)	v (m/s)	ρ (kg/m^3)	T (K)
Preshocked nitrogen	6.0	0	0	30.46	650.0
Postshocked nitrogen	9.096	−160.3	0	40.38	736.2
n-Dodecane	6.0	0	0	419.9	650.0

theoretically proven and confirmed through numerical experiments involving algebraic problems and hyperbolic conservation laws.

(2) Several numerical experiments indicate that this scheme is more efficient in terms of error reduction versus CPU time compared to traditional third-order schemes and, in most cases, even outperforms classical higher-order WENO schemes (WENO5-JS).

(3) It allows for higher values of the CFL number in complex problems.

Moreover, an Harten-Lax-van Leer contact (HLLC) Riemann solver is applied, and additional details can be found in Ref. [88].

In summary, the adoption of the WENO3-type scheme, along with finer meshes, allows for robust, compact, easily implemented, and accurate studies of complex shock-droplet interactions across a wide range of conditions. The effects of mesh resolution and validations are thoroughly compared with results obtained using WENO5, as detailed in Sec. II C and Appendixes D and E.

C. Verification of shock interaction with a two-dimensional cylindrical fuel column

This section focuses on the validation of shock interaction with a cylindrical fuel column, taking into account various factors such as mesh resolution, computational domain, boundary conditions, and the chosen numerical scheme.

To generate numerical schlieren images, we employ the following formula to define the pseudoschlieren value:

$$\emptyset = \exp\left(-C\frac{|\nabla\rho| + A}{B + A}\right). \tag{12}$$

The pseudoschlieren value, denoted as $\emptyset$, is determined using the formula $|\nabla\rho| = [(\partial\rho/\partial \mathrm{x})^2 + (\partial\rho/\partial \mathrm{y})^2]^{1/2}$, where three adjustable parameters, A, B, and C, influence its calculation. Typically, A is set to zero, and B equals $|\nabla\rho|_{\max}$, gradually leading to $\emptyset = \exp(-C|\nabla\rho|/|\nabla\rho|_{\max})$. The gray values displayed in the schlieren images are fine-tuned based on the approach recommended in Ref. [22]. It is important to note that the constant "C" plays a role here, taking the value of 600 for light fluids (such as helium) and 120 for heavy fluids (like R22). In the case of shock interaction with a cylindrical fuel column, C is set to 600 for the nitrogen environment and 120 for the n-dodecane cylinder.

1. Detailed evolution of shock interaction with a cylinder at near-critical conditions

We conduct a validation study to investigate the evolution of shock interaction with an n-dodecane cylinder at near-critical conditions in a nitrogen environment. The parameters for this study closely match those in Ref. [52], with the exception of a finer mesh resolution of 0.115 mm in the region where $z = -160$ mm and 160 mm, compared to their 0.23 mm. The initial conditions, which include thermodynamic parameters, cylinder position, diameter, boundary conditions, and the computational domain with the shaded fine-mesh region, are presented in Fig. 2 and Table I.

In this scenario, we aim to illustrate the shock interaction with a near-critical droplet. This interaction occurs at a supercritical pressure and subcritical temperature, placing the n-dodecane in a liquidlike supercritical state. The critical properties of n-dodecane are defined by a critical pressure (p_c) of 1.82 MPa and a critical temperature (T_c) of 658.1 K. As a result, the n-dodecane droplet begins in a supercritical state where it is pressurized at subcritical temperature.

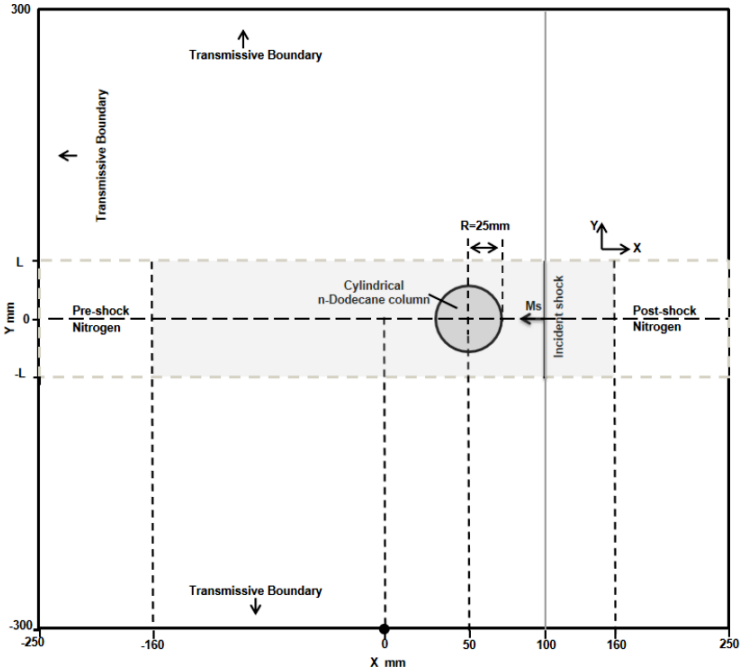

FIG. 2. Scheme of the computational domain for the shock-cylinder interaction at near-critical conditions.

For the nitrogen environment, it is crucial to note that its temperature exceeds the critical temperature, and its pressure is above the critical pressure. Nitrogen's critical properties are characterized by a critical pressure (p_c) of 3.369 MPa and a critical temperature (T_c) of 126.2 K. The shock wave in this environment maintains a Mach number of 1.2. Reference [78] provides the NASA polynomial parameters, and for this part of the study, we employ OWENO3 as the numerical scheme.

In this section, our primary focus is to analyze the morphological aspects of shock interaction with a pure cylinder. While Boyd and Jarrahbashi provide a useful overview of the main features [52], we seek a more comprehensive description of the morphology at near-critical conditions.

As illustrated in Fig. 3, the incident shock wave (IS) initially passes the upstream pole and travels towards the downstream pole. The time instance when the shock contacts the upstream surface of the cylinder (USC) is defined as 0μs. Once the IS reaches the USC, it leads to the formation of a curved refracted shock (TS) within the cylinder and a shock reflection (RS) from the USC. The RS in n-dodecane is slower than the IS due to the lower speed of sound (SoS).

Around 105 μs, surface-vertical diffracted shocks (DSs) emerge on the downstream surface of the cylinder (DSC). The sweep of these DSs subsequently induces the generation of an incident diffracted transmitted shock (DTS). To balance the pressure difference between the converging (refracted) transmitted shock (TS1) and the incident DTS, a new small shock (NSS1) is formed. This leads to the gradual reduction of both the angle between the DTS and the TS1 and the undisturbed zone (UZ).

By 115 μs, the crossover point of the incident shock is noticeable, and the convergence of NSS1, DTS, and TS1 results in the formation of high-pressure zones. At 120 μs, the converged refracted shock becomes evident, and by 125 μs, the original TS1 impinges on the Mach stem (generated by the internal convergence of the DTS), creating an even higher pressure oval region (OZ).

At 130 μs, it is observed that the newly formed internal Mach stem (IMS, representing one edge of the oval region) impinges on the downstream interface and generates a transmitted Mach stem (TMS). Gradually, a surface jet formation (JF) is observed at 185 μs. This evolution, from the

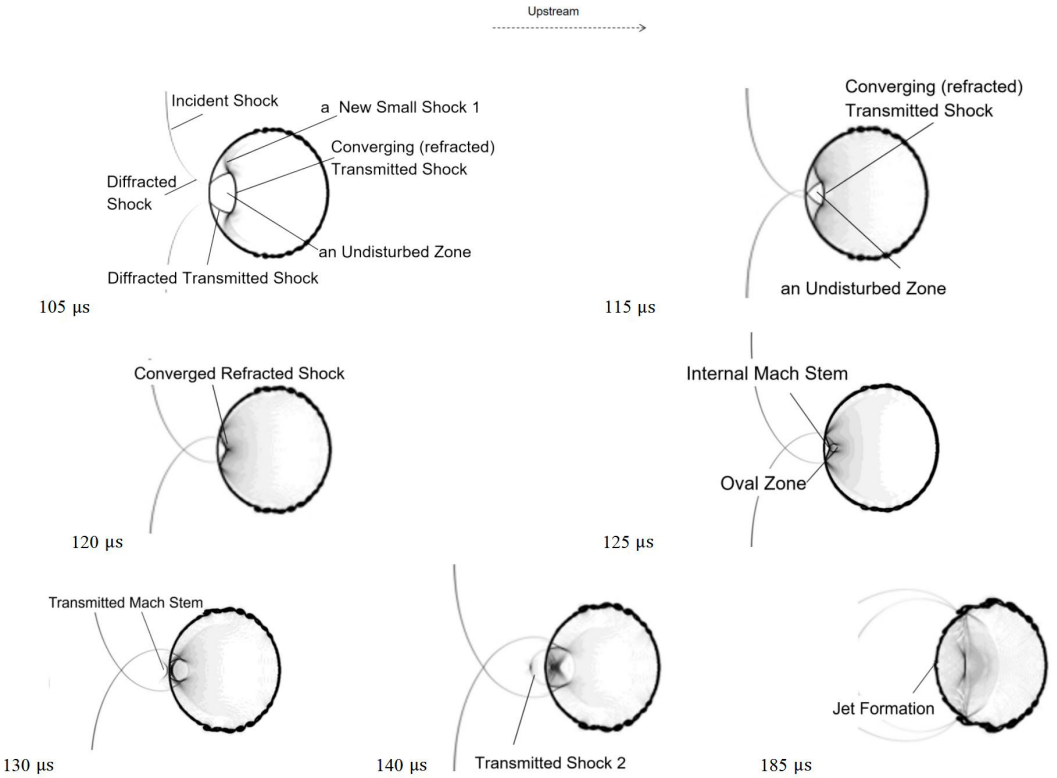

(a) Typical views at the time: 105 μs, 115 μs, 120 μs, 125 μs, 130 μs, 140 μs, 185 μs.

(b) Enlarged view at the relevant time: 125 μs, 130 μs.

FIG. 3. Representative view of the flow morphology in a shock-accelerated cylinder. Typical views at the time (a) 105 μs–185 μs, (b) 125 μs, 130 μs.

converged refracted shock (CRS) focal wedge, to the OZ, to the TMS, represents the mechanism behind the development of the surface jet.

It is important to note that this morphological evolution is akin to the cases of shock interaction with a heavy bubble (e.g., R22, SF_6, Kr) studied by various researchers, such as Haas and Sturtevant [21], Jacobs [89], Zhai *et al.* [90], Zou *et al.* [91], Fan *et al.* [92], and Guan *et al.* [93]. The process depicted in Fig. 3 aligns well with the findings in Ref. [52], providing qualitative validation for our methods and affirming that the mesh resolution is sufficient to capture these intricate features. Further discussion and details are provided in Sec. III A.

Additionally, we conducted a quantitative comparison by examining pressure distributions and comparing them with the results presented in the reference study. In Fig. 4, the black lines represent the pressure distribution achieved using a mesh resolution of 0.115 mm and the OWENO3 numerical scheme. The pressure distribution closely matches the reference data, although there is a minor

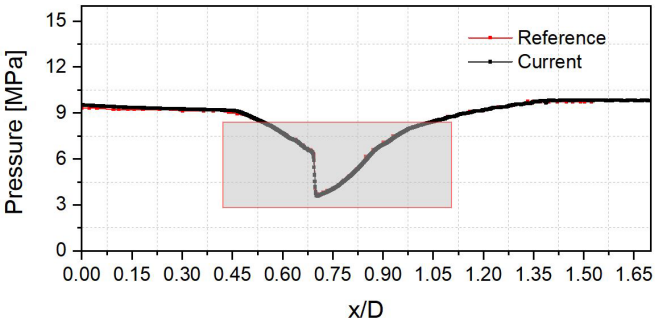

(a)

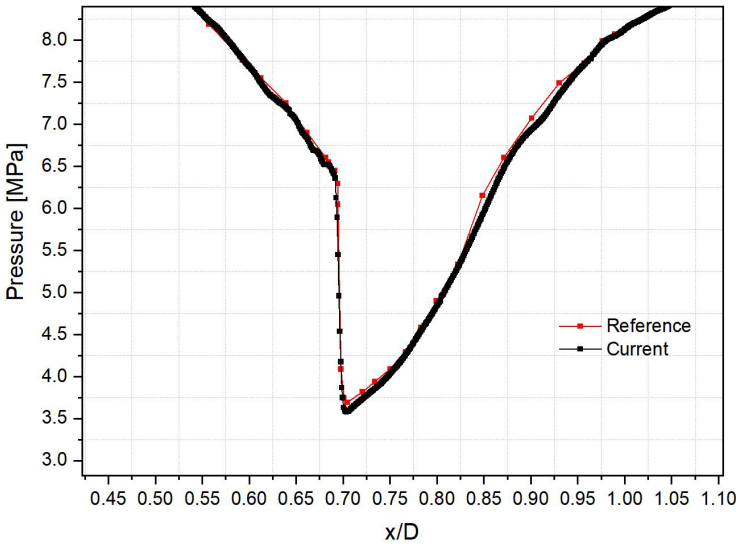

(b)

FIG. 4. The pressure distributions of the current case and the reference case at time 185 μs.

pressure difference (less than 1%) near the discontinuity region. This discrepancy can be attributed to the weak pressure oscillations that occur in the vicinity of the discontinuity region. For further validation, a case involving shock interaction with a helium bubble is provided in Appendix E.

In summary, we have successfully demonstrated that our numerical scheme produces accurate results and that the current mesh resolution is sufficient to capture the essential features of near-critical shock-cylinder interactions.

2. Effects of mesh resolution and numerical scheme on near-critical shock-cylinder interactions

Mesh resolution studies are of particular importance, as essential flow characteristics may still be observed with coarser mesh resolutions. We consider meshes up to four times finer than 0.23 mm.

In Figs. 5 and 6, we present simulations conducted within a larger computational domain with coarser meshes near the boundaries. In this setup, wave reflections from the top and bottom walls are suppressed to isolate the planar shock effects. We compare various mesh resolutions and OWENO3 and WENO3, assessing the level of dissipation. The results demonstrate that OWENO3 yields improved results with reduced dissipation compared to WENO3. OWENO3, with a mesh

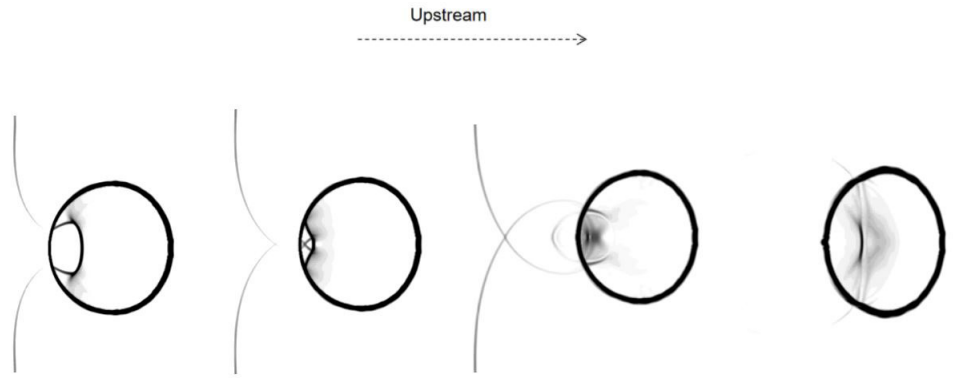

(a) Large domain with WENO3 (mesh resolution: 0.23 mm).

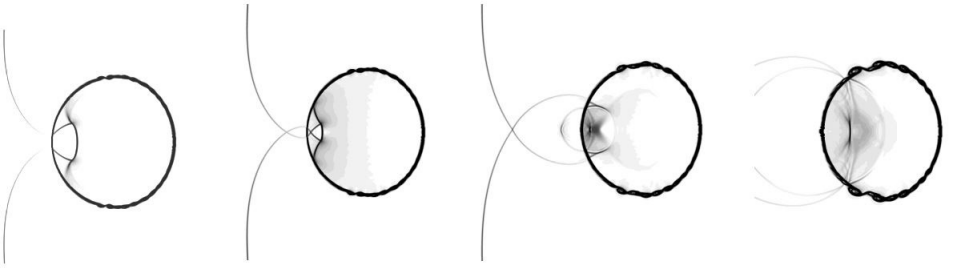

(b) Large domain with WENO3 (mesh resolution: 0.115 mm).

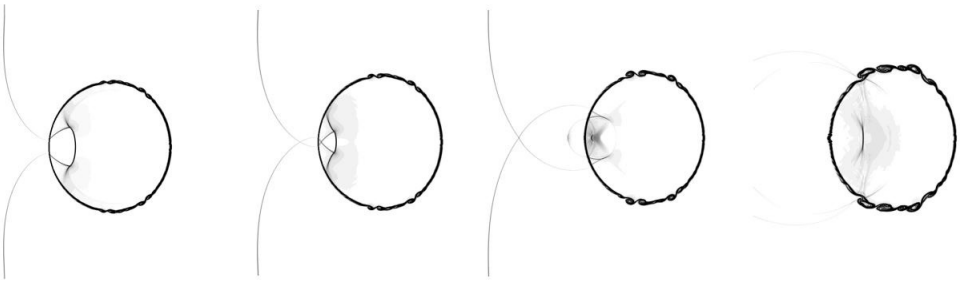

(c) Large domain with WENO3 (mesh resolution: 0.0767 mm).

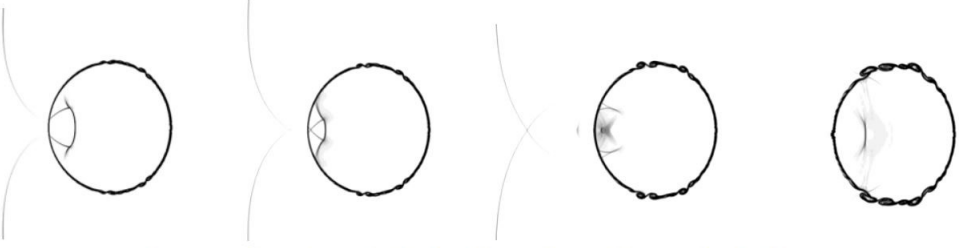

(d) Large domain with WENO3 (mesh resolution: 0.0575 mm).

FIG. 5. The shock *n*-dodecane cylinder interaction within the large domain at times 105, 115, 140, and 185 μs (from left to right). WENO3 with a mesh resolution of (a) 0.23 mm, (b) 0.115 mm, (c) 0.076 mm, (d) 0.0575 mm.

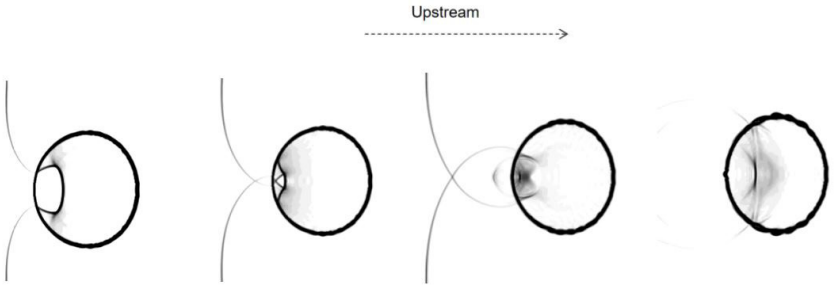

(a) Large domain with OWENO3 (mesh resolution: 0.23 mm).

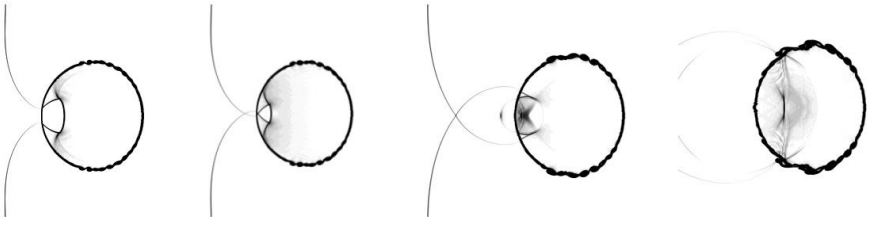

(b) Large domain with OWENO3 (mesh resolution: 0.115 mm).

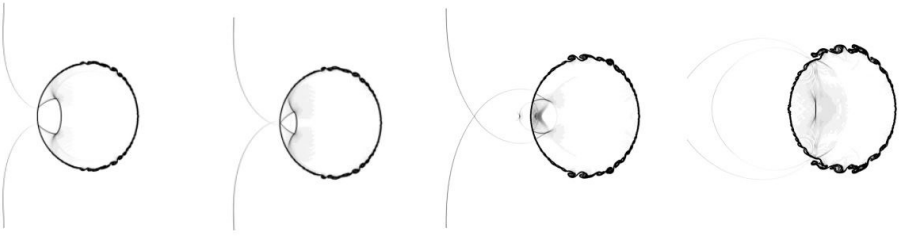

(c) Large domain with OWENO3 (mesh resolution: 0.0767 mm).

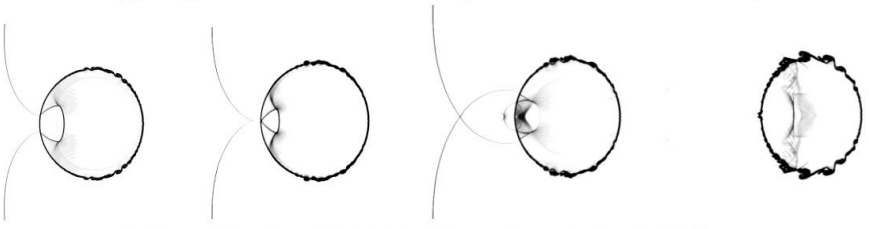

(d) Large domain with OWENO3 (mesh resolution: 0.0575 mm).

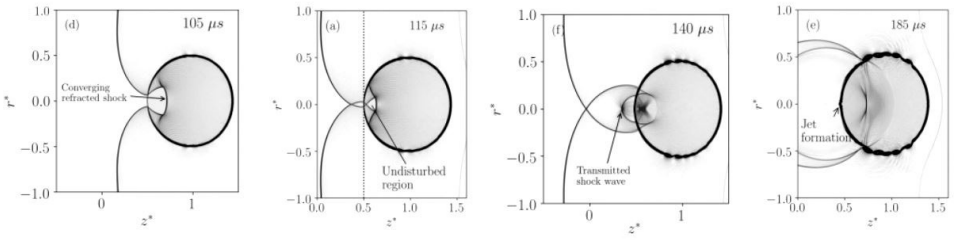

(e) Reference results [52], large domain with WENO5 (mesh resolution: 0.23 mm).

FIG. 6. The shock *n*-dodecane cylinder interaction within the large domain at times 105, 115, 140, and 185 μs (from left to right). OWENO3 with a mesh resolution of (a) 0.23 mm, (b) 0.115 mm, (c) 0.0767 mm, (d) 0.0575 mm. WENO5 with a mesh resolution of (e) 0.23 mm from Ref. [52]. Reproduced from Ref. [52].

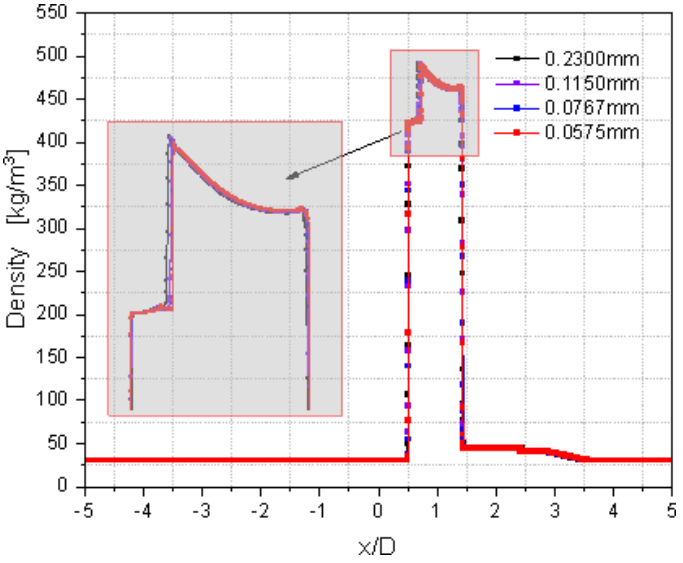

FIG. 7. Grid convergence test on the shock *n*-dodecane cylinder interaction by OWENO3 within large domain at time 143 μs.

resolution of 0.115 mm, can provide results that are comparable to those obtained with WENO5 from Ref. [52].

For assessing mesh independence, we also analyze the density distribution, as depicted in Fig. 7. The density distributions directly display the contact positions of both fluids and converge to the red line with the finest mesh resolution of 0.0575 mm. Notably, there are minimal differences between the results obtained with mesh resolutions of 0.115 and 0.0575 mm. Therefore, for a well-balanced consideration of accuracy and computational efficiency, a mesh resolution of 0.115 mm is a suitable choice.

In this way, a high mesh resolution, exceeding 434 computational cells per droplet diameter (diameter = 50 mm), is employed. This translates to more than 0.87 billion equivalent finite volumes for the entire three-dimensional *n*-dodecane droplet simulation, potentially making it the largest simulation of *n*-dodecane at near-critical conditions reported to date.

Even finer meshes would likely capture more small-scale structures, as demonstrated in our mesh independence study. However, these tiny vortex structures are ephemeral in reality, quickly dissipating due to physical processes (physical diffusion). In simulations, numerical viscosity (inherent to the simulation scheme) also acts to dissipate these structures rapidly, preventing them from influencing the larger structures of interest. In essence, these small structures become so short-lived that they are negligible. As in Refs. [52,82], viscous terms are insignificant in short-duration processes with rapid shock interactions.

Our results accurately capture the interface structures and shock wave patterns (Fig. 6) when compared with reference data [52]. In cases where different mesh resolutions are used, the main roll-up structures are captured in a comparable manner. As discussed above, while finer meshes might reveal even smaller two-phase structures, these would likely have minimal influence on the dominant processes governing the deformation of the two-phase interface and the evolution of shock waves. Therefore, the focus on capturing the key characteristics and conducting mesh independence studies is justified.

Furthermore, the relative total energy error values are calculated at $t = 105\,\mu s$, where $\epsilon = |(\int_\Omega (\rho E)^t - \int_\Omega (\rho E)^0)/\int_\Omega (\rho E)^0|$. The values are 0.0405, 0.0219, 00110, and 0.0009 for cases with mesh resolution of 0.2300, 0.1150, 0.0767, and 0.0575 mm, respectively. It is consistent with Refs. [11,51,66] that the total energy conservation error decreases with increasing resolution.

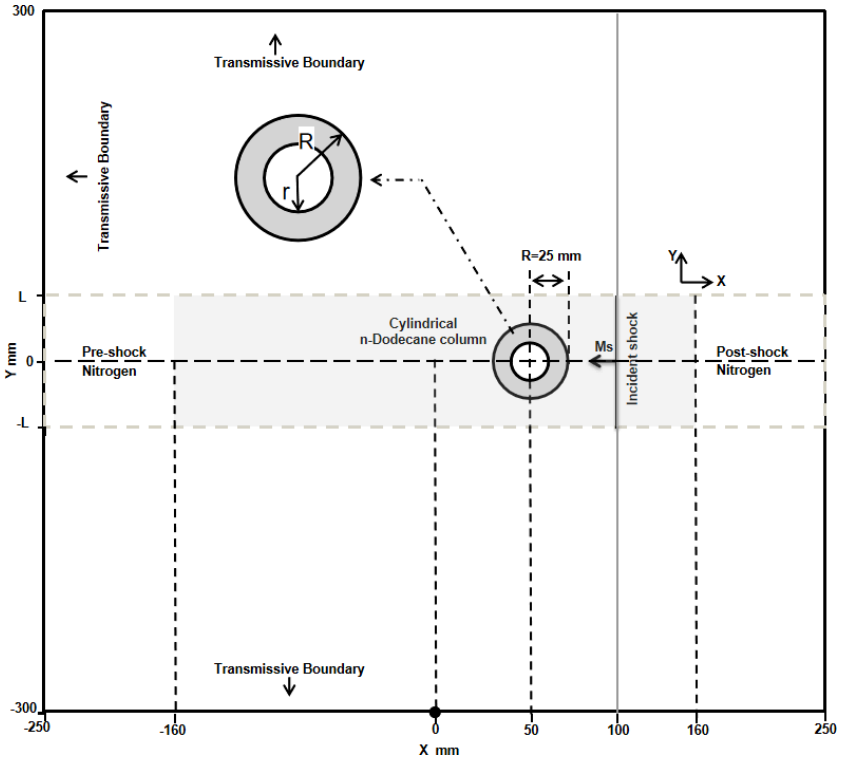

FIG. 8. The schematic for the computational domain of the shock-cylinder ring interaction.

Additionally, we also consider various cases involving different computational domains and boundary conditions to demonstrate the robustness and accuracy of our current numerical scheme (see Appendixes D and E for these additional cases).

III. RESULTS AND DISCUSSION

A. Analysis of a cylinder with an internal gas cavity

As depicted in Fig. 8, a gaseous cavity is situated at the center of the cylindrical column with a diameter $r/R = 0.5$. The thermodynamic properties, such as pressure, velocity, density, and temperature, of the internal gas bubble are maintained consistent with the preshock nitrogen environment.

One way to define the characteristics of the shock interactions in such cases is by considering the speed-of-sound (SoS) ratio, as suggested by Ref. [21]. In the present scenarios, the speed of sound (c_S) in the surrounding preshock nitrogen environment is greater than that in the n-dodecane cylinder (c_D). This results in a SoS ratio ($n = c_S/c_D$) greater than 1, indicating a convergent situation, where the refracted shock within the n-dodecane cylinder is slower than the incident shock wave. This is analogous to the convergent situation seen in shock–R22 bubble cases, in contrast to the divergent situation in shock–helium bubble cases. Additionally, $\delta Z > 0$ is a typical description of a convergent case [28].

The acoustic impedance mismatch across the material interface between the n-dodecane cylinder and the surrounding nitrogen fluid, denoted as $\delta Z = (\rho c)_D - (\rho c)_S > 10^5$, significantly influences the transition of a shock wave across the interface. In the current cases, when the incident shock reaches the upstream surface of the cylinder (USC), it forms a refracted wave as well as a reflected shock wave due to the fact that $\delta Z \gg 0$ (similar to shock–R22 bubble cases). Conversely, if there

is no gas cavity within the cylinder (a pure cylinder), and the refracted shock travels through the cylinder to the downstream surface of the cylinder (DSC), an opposite impedance mismatch occurs with $\delta Z \ll 0$, causing the reflected wave to become a rarefaction wave for the current case, much like in shock–R22 bubble cases.

Another important parameter to consider is the Atwood number (A), which is defined as $A = (\rho_D - \rho_S)/(\rho_D + \rho_S)$ and characterizes the effect of density variation between the *n*-dodecane cylinder and the surrounding nitrogen fluid. The dimensionless time t^* corresponds to the simulated physical time t, divided by an arbitrarily chosen reference time $t_{\text{ref}} = 8.68 \times 10^{-6}$ s.

1. Early wave pattern evolution of the shock-cylinder ring interaction at near-critical conditions

This section offers an in-depth analysis of the early wave pattern evolution during the interaction between a shock and a cylindrical ring at near-critical conditions. Figure 9(a) illustrates the initial phase of the interaction. The incident shock (IS) passes over the USC, leading to the generation of the reflected shock (RS) and the converging (refracted) transmitted shock (TS1). Simultaneously, the cylinder undergoes deformation and initiates downstream movement. These processes are designated as "1."

Subsequently, after TS1 encounters the upstream surface of the embedded gas bubble (USB), the angle between USB and TS1 begins to increase from zero. During this early stage, two significant events occur:

(1) The second reflected rarefaction wave (RR) is generated.

(2) The diverging (refracted) transmitted shock 2 (TS2) begins to take shape.

Both begin at relatively small angles. Simultaneously, the embedded gas bubble also starts moving and deforming downstream. These processes are marked as "2." These early wave pattern changes, constituting the inner shock-bubble interaction process, resemble typical refraction processes, akin to shock interactions with lighter gas bubbles, as seen in shock–helium bubble cases.

Given the higher impedance of the *n*-dodecane cylinder compared to nitrogen, TS2 inside the nitrogen bubble moves faster than TS1 inside the cylinder. This results in the generation of a side shock (SS) and a new shock 1 (NS1), as depicted in Fig. 9(b). SS is often referred to as the free-precursor shock wave (FPS) in the literature [57]. At this stage, TS1, SS, NS1, and reflected shock 2 (RS2) converge at a point marked as "P4," which resembles the free precursor refraction (FPR) phenomenon [57,94].

As RS2 and SS propagate in different directions, they form an angle between them. Consequently, as shown in Fig. 9(c), P4 is replaced by two distinct intersection points (P2) and the formation of a Mach stem. This wave pattern is reminiscent of the twin von Neumann refraction (TNR) [94].

In Fig. 9(d), as TS2 reaches the downstream surface of the bubble (DSB), it gives rise to a transmitted shock (TS3) and a reflected shock (RS3), both traveling in opposite directions. The points of intersection for these three shock waves (P3) arise from the movement of TS1. Moving on to Fig. 9(e), both the transmitted wave TS5 and the reflected wave RS5 emerge near the USB. RS2 refracts from the DSC, forming a transmitted shock from RS2 (TRS2). Additionally, diffracted shock waves form a crossover point outside the DSC. Furthermore, as depicted in Fig. 9(f), TS3 passes through the DSC, creating a fourth transmitted shock (TS4) and a rarefaction wave heading towards the DSB. The diffracted shock, TRS2, and TS4 comprise the primary structures of the wave pattern outside the cylinder ring. Inside the cylinder ring, further development of NS1, TS1, the rarefaction wave of TS3, and other waves form a more intricate pattern of waves.

A comparison between Fig. 3 and Figs. 9(a)–9(g) reveals that the evolution of the outer cylinder surface in the ring case mirrors that of the pure cylinder case, akin to shock interactions with heavy fluids [21,89–93]. The two-phase interface between the cylinder ring and the outer nitrogen environment resembles the previous results of a pure cylinder. However, the jet formation at the DSC is diminished, attributed to the newly formed complex wave pattern interaction, such as the interaction between P3 and DSC.

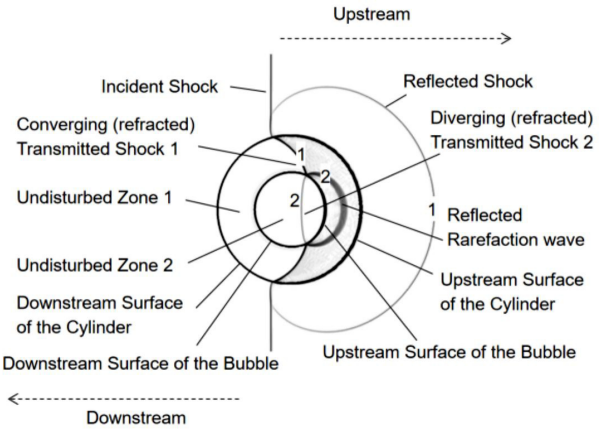

(a) t^*=9.

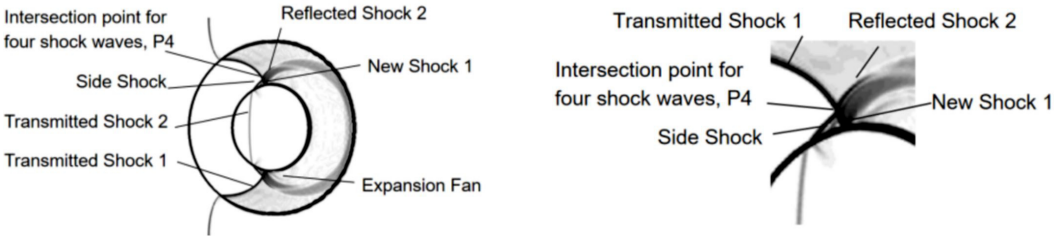

(b) t^*=11.

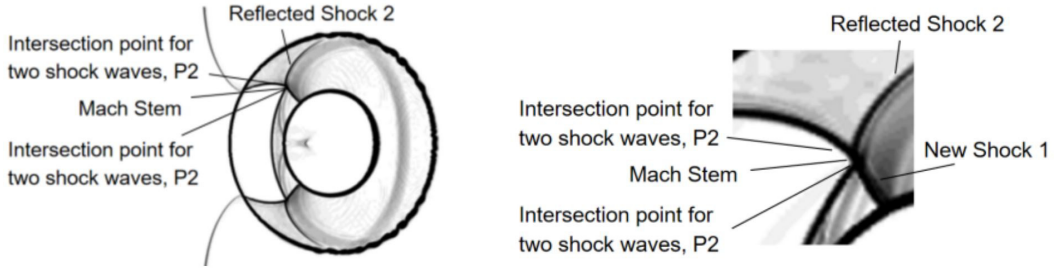

(c) t^*=13.

FIG. 9. Representative view of the flow morphology and wave pattern evolution in a shock-accelerated cylinder ring at near-critical conditions.

Figures 9(a)–9(g) show the progression of the shock wave pattern in a case involving a gas cavity. Over time, the USB presses into the center of the nitrogen, taking on a kidney shape, reminiscent of shock-accelerated light bubbles (shock helium bubble). It is noteworthy that the internal shock wave pattern bears resemblances to shock–helium bubble (light gas) interaction cases. In the current cylinder ring scenario, the IS of shock–helium bubble cases is replaced by TS1, a reasonable substitution given the shared attributes of "heavy-light layer" cases.

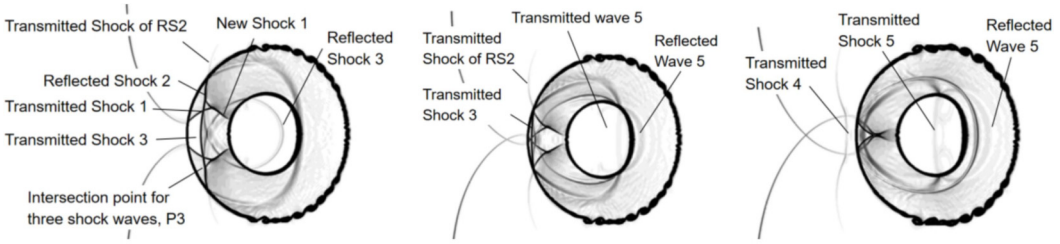

(d) t^*=15. (e) t^*=16. (f) t^*=17.

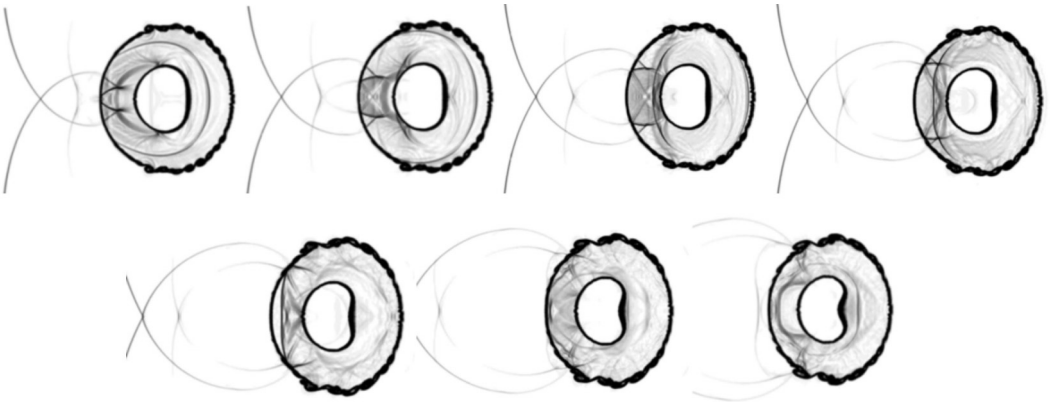

(g) t^*=18, 19, 20, 21, 22, 23, 24 (from top left to bottom right).

FIG. 9. (*Continued*).

2. Late development of pure cylinder and cylinder ring

In the later stages of the evolution process, the internal kidney-shaped gas bubble continues to move downstream, as seen in Figs. 10(a)–10(g). For the internal bubble region in the case with a cavity, it is observed that a cylindrical jet forms and grows over time, displaying similarities to the shock–helium bubble case. Initially, a mushroomlike structure containing a pair of vortices [Fig. 10(h)] develops in the downstream direction and then reaches the DSB [Fig. 10(i)]. The distance between the USB and DSB decreases, and the internal bubble gradually splits into two smaller bubbles [Fig. 10(j)]. Subsequently, two pairs of vortices move in opposite directions and spray separately into two nitrogen bubbles, forming several smaller jets [Fig. 10(k)]. These newly formed small curved jets spin around and move towards the cylinder-bubble interface again, rolling the small bubble interface upstream. Finally, the curved interfaces form another mushroom containing a pair of vortices and tend to impact the USB [Fig. 10(l)]. These processes introduce complex impacts and interactions into the internal region of an originally pure cylinder, enhancing the mixing of gas and cylinder.

Additionally, in a shocked pure cylinder, the high pressures (OZ) generated by the shock focusing inside the cylinder lead to the formation of an outward jet, as shown in Fig. 3. Gradually, the induced jet approaches the DSC of a pure cylinder. However, in the case with a cavity, the internal bubble alters the motion of the shock waves, disrupting the OZ and reducing the tendency for jet formation, as also observed in Fig. 9.

In the literature [5,33,47–49,55–59], investigations of configurations similar to ours, but under subcritical conditions, are presented. We compare our results with existing subcritical studies [57,59] to understand the influence of near-critical conditions. Both Feng *et al.* [57] (gas cylinder)

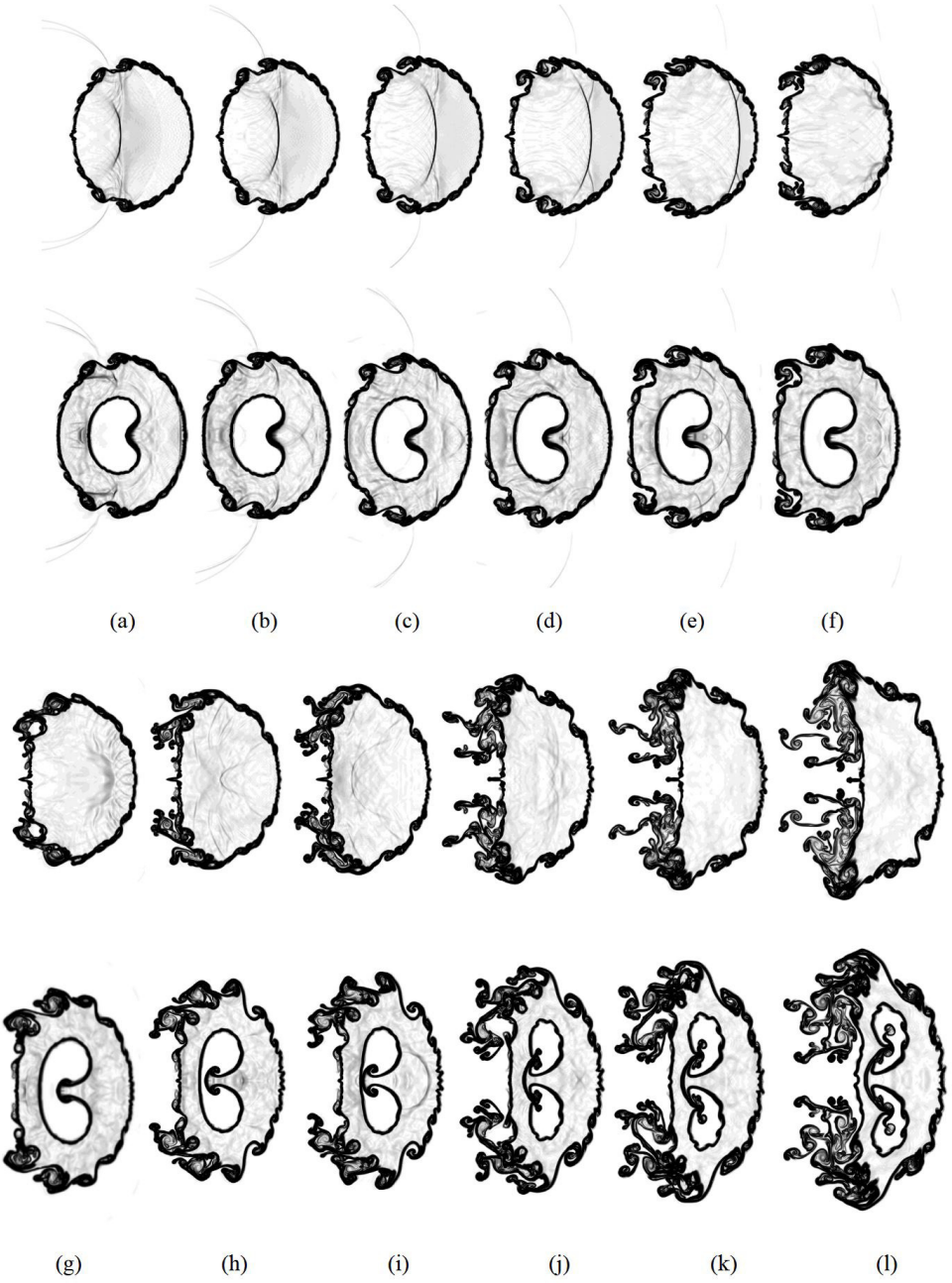

FIG. 10. Late evolution of the jet formation of pure cylinder and cylinder ring at near-critical conditions at $t^* =$ (a) 27, (b) 29, (c) 31, (d) 33, (e) 35, (f) 37, (g) 40, (h) 46, (i) 49, (j) 56, (k) 60, and (l) 66.

and Xiang and Wang [59] (water column) employed configurations with comparable Mach numbers to ours.

In the initial stages, the wave patterns observed in our near-critical case (our Figs. 3 and 9) resembled those reported by Feng *et al.* [57] under subcritical conditions (their Figs. 4 and 7). This suggests similar shock interactions (Mach stem, transmitted shock, shock focusing, etc.).

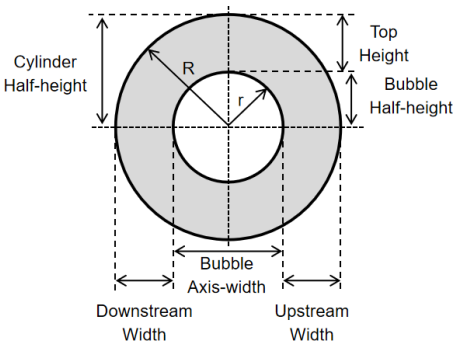

FIG. 11. The diagram of the measured parameters (sketch map).

However, the deformation behavior of our near-critical cylinder diverged significantly from the SF_6 gas cylinder response under subcritical conditions [57].

Interestingly, our near-critical wave patterns (our Figs. 3 and 9) differed from those observed by Xiang and Wang [59] for a subcritical water column without a cavity (their Fig. 5). However, the two-phase structures observed in their study with a cavity (their Figs. 14 and 16) exhibited a strong resemblance to the deformation behavior of our near-critical cylinder (our Fig. 10).

These comparisons lead to the following conclusions:

(i) Early-stage wave patterns in our near-critical cylinder case are similar to subcritical SF_6 gas cylinder cases [57].

(ii) The deformation behavior of our near-critical cylinder deviates significantly from the classical subcritical SF_6 gas cylinder behavior shown in Ref. [57].

(iii) While the wave patterns in our case differ from subcritical water columns, the deformation behavior of our near-critical cylinder closely resembles that of a subcritical water column in air as investigated by Xiang and Wang [59].

3. Quantitative analysis of shock-cylinder ring interaction

Figures 11 and 12 present a quantitative analysis of the shock-cylinder ring interaction, focusing on the evolution of key parameters. These parameters include the top height of the cylinder ring, the half-height of the internal bubble, the width of the inner bubble, the upstream width of the cylinder ring, and the downstream width of the cylinder ring. This analysis allows for a detailed understanding of the complex interactions taking place.

Top height of the cylinder ring (green line). After T1, the IS induces Richtmyer-Meshkov instabilities (RMIs), leading to the development of concave-convex structures in the two-phase interface. These instability structures grow and rotate forward, resulting in variations in the top height of the cylinder ring.

Half-height of the internal bubble (purple line). Following T2, this parameter initially remains relatively flat. However, as transmitted shock 1 (TS1) passes the semicircle of the internal bubble, it begins to decrease due to the converging TS1. Subsequently, the internal bubble takes on a kidney shape and the height gradually increases.

Half-height of the cylinder ring (dark yellow line). This parameter is the sum of the top height of the cylinder ring and the half-height of the internal bubble, which reflects the behavior of the top height of the cylinder ring and closely follows the same trends.

Upstream width of the cylinder ring (black line). The width decreases shortly after T1. Subsequently, as TS1 interacts with the USB, the width tends to increase, mainly due to the formation of the kidney-shaped internal bubble.

Width of the internal bubble (blue line). The width of the internal bubble begins to decrease after T2.

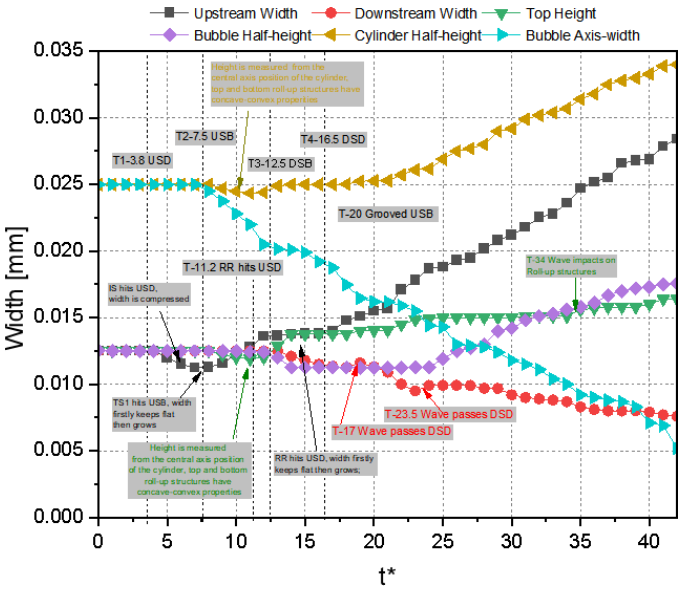

FIG. 12. The evolution histories of the measured parameters of the cylinder ring. T1–T4 separately represent four important times: IS reaches the USC, TS1 reaches the USB, TS2 reaches the DSB, and TS3 reaches the DSC. The dimensionless time used here is calculated from the beginning and is normalized by 8.68×10^{-6} s. The heights are measured at the line $x = 50$ mm.

Downstream width of the cylinder ring (red line). After TS2 passes the DSB, the downstream width of the cylinder ring decreases. It slightly increases after TS3 passes the DSC, but then continues to decrease. Another TS wave passing the DSC induces a small increase. Subsequently, the cylinder ring appears to stretch in the normal direction, and the width between DSC and DSB decreases. A decreased jet formation near the DSC is also observed, which differs from the behavior in shock interaction with a pure cylinder.

B. Quantitative comparison between pure cylinder and cylinder ring

1. Quantitative analysis of vorticity dynamics

Baroclinic vorticity production arises from unbalanced gradients between density and pressure, particularly when the IS or TS passes the two-phase interface. This phenomenon plays a crucial role in RMI and the induction of turbulent mixing. Figure 13 shows the process of vortex generation by baroclinic production in the shock-cylinder ring interaction. The vorticity transport equation is represented by $\mathrm{D}\omega/\mathrm{D}t = 1/\rho^2 \nabla\rho \times \nabla p$. The angle between the pressure gradient and density gradient is most significant near the top and bottom vertices of the cylinder, as depicted in Fig. 14(a). The vortex pairs develop near the pits and bumps (peaks and valleys) of the outer cylinder, gradually increasing in intensity. Notably, in both cases with and without a cavity, vortex growth and rotation are observed near the top and bottom vertices of the cylinder, ultimately forming prominent wake roll-up structures [Figs. 13(a) and 13(b)]. Positive and negative vortices predominantly form on the upper and lower surfaces of the outer cylinder, respectively.

In the pure cylinder case (without a cavity), a jet is evident near the DSC, with the vertex of the jet being particularly noticeable in the equator region. In contrast, in the case with a cavity, the outer jet is suppressed [Fig. 13(c)], but baroclinic effects caused by shock interaction with the internal light bubble within the heavy cylinder environment lead to additional vorticity generation. The newly formed internal mushroom jet is associated with a pair of vortices characterized by opposite spin

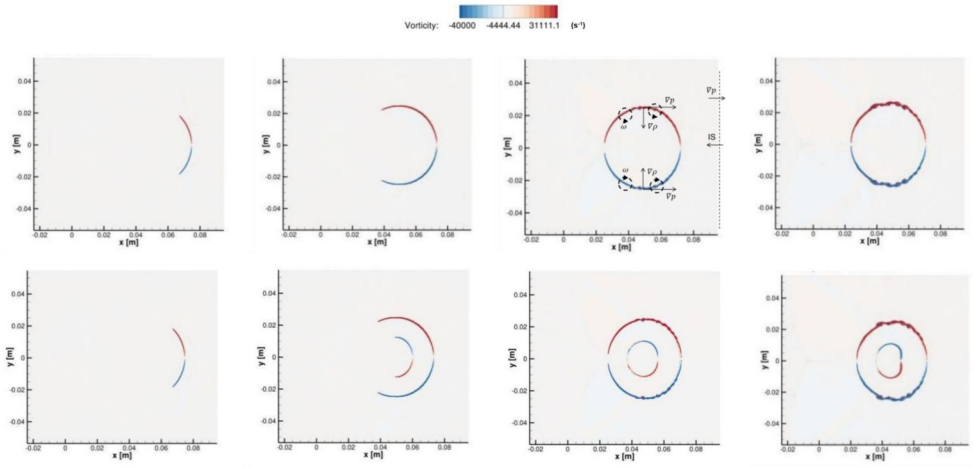

(a) t^*=5, 10, 15, 20 (from left to right).

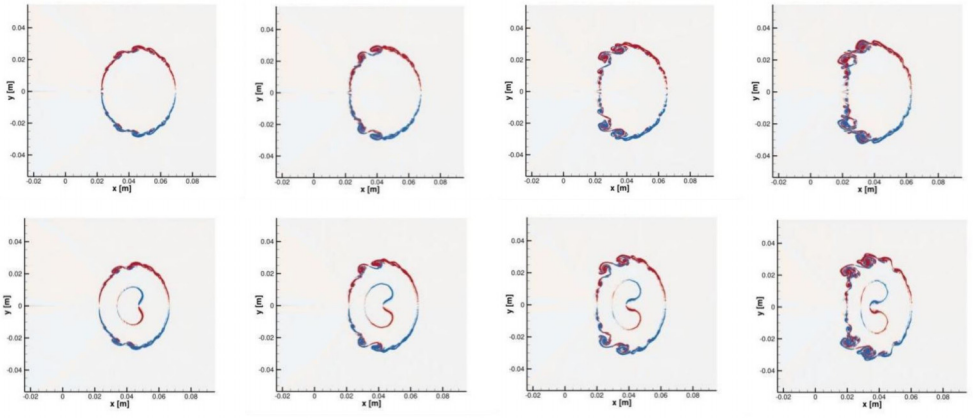

(b) t^*=25, 30, 35, 40 (from left to right).

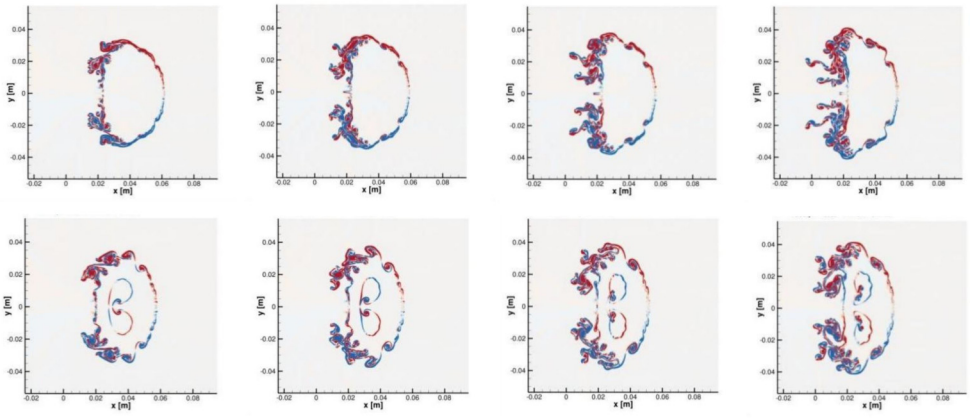

(c) t^*=45, 50, 55, 60 (from left to right).

FIG. 13. Schematic diagram of vorticity generation in the shock-cylinder ring interaction (vorticity restricted to the same range of values). For t*, (a) 5, 10, 15, 20, (b) 25, 30, 35, 40, (c) 45, 50, 55, 60, (d) 65, 70, 75, 80.

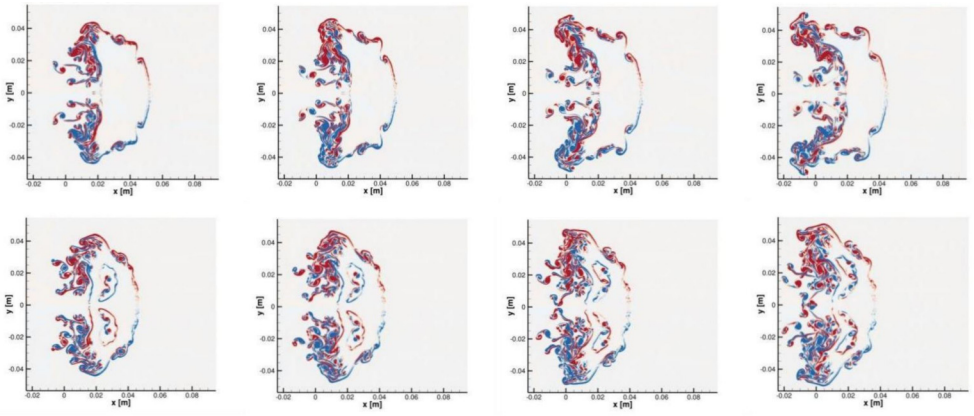

(d) t^*=65, 70, 75, 80 (from left to right).

FIG. 13. (*Continued*).

directions [Fig. 13(c)]. This jet carries roll-up vortex structures. Vortex patterns of negative and positive vorticity primarily form on the upper and lower surfaces of the inner bubble, respectively, which is the opposite pattern to that observed on the outer cylinder.

In Fig. 14, we examine the impact of an internal gas cavity on the time evolution of enstrophy in the shock wave–cylinder interaction at near-critical conditions. Enstrophy, which accounts for compressibility, is presented in a mass-averaged form as $(\int \rho\omega^2 dxdy)/(\int \rho dxdy)$. For both cases, with and without a cavity, the enstrophy values are initially zero before the shock wave reaches the USC. Subsequently, they increase almost linearly. In the early stage ($t^* < 36$), enstrophy in both cases is similar, primarily due to the negligible enstrophy of the internal bubble. However, once the internal bubble forms a jet, the enstrophy of the cylinder ring case becomes greater than that of the pure cylinder case. During a narrow time interval ($63 < t^* < 69$), the enstrophy of the pure cylinder case surpasses that of the cylinder ring case. This shift could be attributed to the formation of a jet

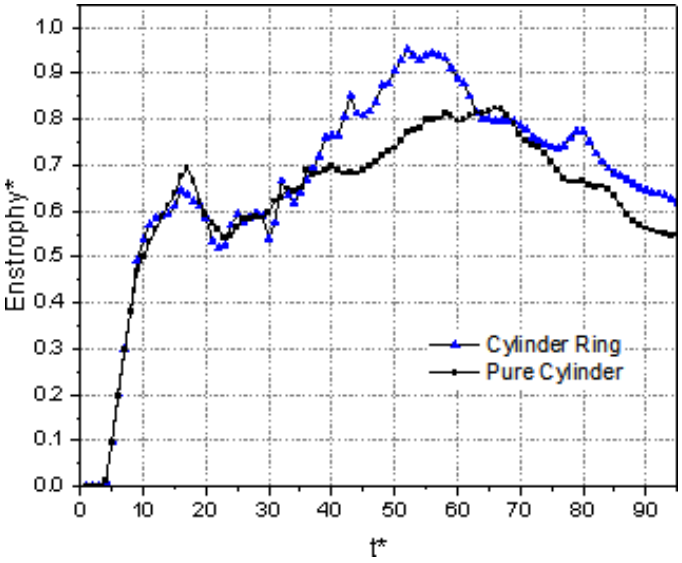

FIG. 14. The evolution of the enstrophy integrated in the domain (normalized by 1×10^8 s^{-2}).

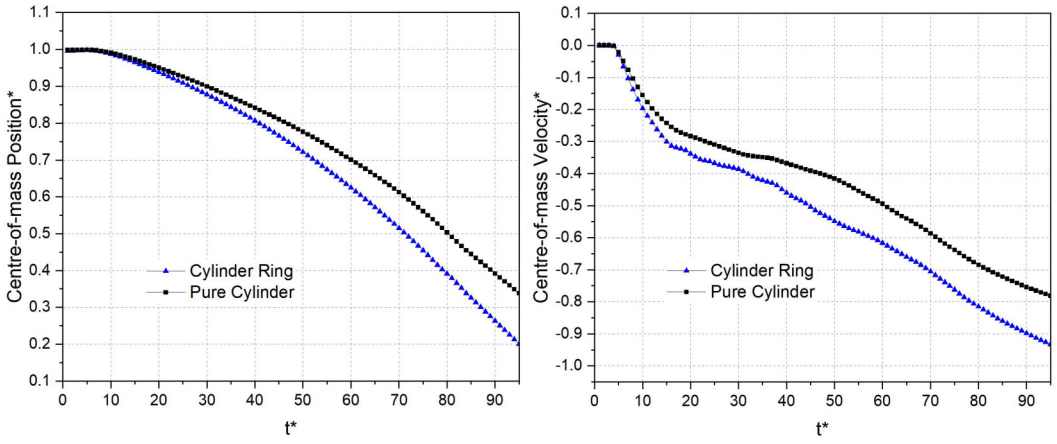

FIG. 15. The drift of the center-of-mass position and velocity (dimensionless by 0.05 m and 100 m/s).

near the downstream surface of the pure cylinder and the role of the internal bubble in accelerating the vorticity consumption process.

As the internal bubble forms additional mushroom structures, which contain more enstrophy, and with the presence of more complex structures near the downstream surface, the trend is reversed, and the enstrophy of the cavity case exceeds that of the pure cylinder case ($t^* > 69$). Overall, the generation of baroclinic vorticity significantly increases enstrophy during the early and intermediate stages of shock wave interaction with the two-phase interface. This enhanced vorticity promotes the mixing of internal and external ambient gases with the fuel cylinder (or ring) and facilitates vorticity energy transfer and consumption, ultimately leading to a reduction in enstrophy strength.

This analysis illustrates how the internal gas cavity influences the enstrophy dynamics in the shock-cylinder ring interaction, particularly in the context of enstrophy generation, transfer, and consumption throughout the interaction process.

2. Drift of the center-of-mass position and velocity

The center-of-mass properties of both the deforming cylinder and the cylinder ring are essential for diagnostics [33] and can be quantitatively analyzed through simulations. Drift analysis involves calculating the center-of-mass position and velocity of these objects as indicated by the following equations:

$$x_c = \frac{\int (1-\xi_{\text{Gas}})\rho \boldsymbol{x} dxdy}{\int (1-\xi_{\text{Gas}})\rho dxdy}, \tag{13}$$

$$u_c = \frac{\int (1-\xi_{\text{Gas}})\rho \boldsymbol{u}\, dxdy}{\int (1-\xi_{\text{Gas}})\rho\, dxdy}. \tag{14}$$

The integration region refers to the entire computational domain.

Figure 15 provides a comparison of the center-of-mass location and velocity between the pure cylinder and the cylinder with an embedded gas cavity. Generally, the center-of-mass location and velocity of the ring are similar to those of the pure cylinder. However, the presence of the gas cavity results in the entire ring moving at a higher velocity compared to the pure cylinder, which can have implications for enhancing the mixing process.

C. Three-dimensional simulation of shock interaction with droplet with and without cavity

In this section, we will conduct three-dimensional simulations of shock interaction with a droplet, under the same conditions as described in Sec. III A. The setup involves using a quarter of the

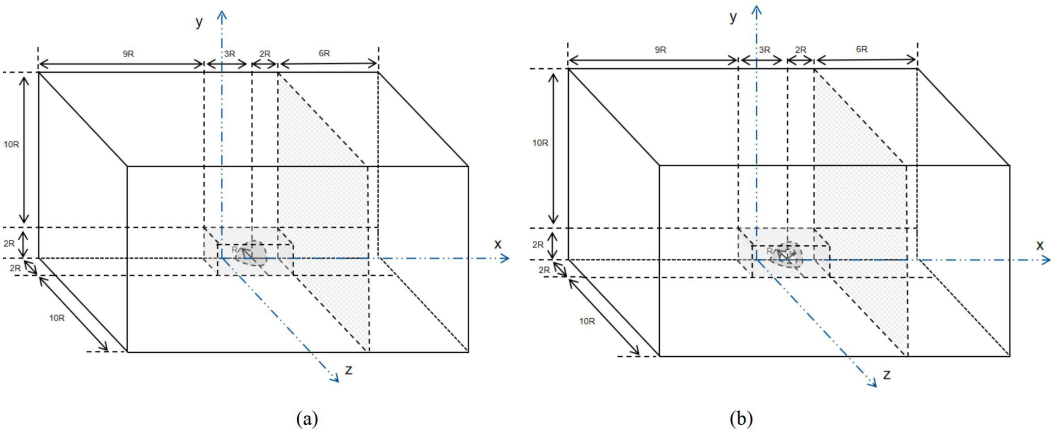

FIG. 16. Schematic of the computational domain for shock interaction with (a) a droplet or (b) a droplet shell.

spherical droplet and a quarter of the droplet shell, as depicted separately in Figs. 16(a) and 16(b), with a diameter ratio of $r/R = 0.5$.

Building upon the insights gained from the two-dimensional results, we will observe the evolution of the shock-droplet interaction. To capture the intricate details of the spherical droplet, a uniform mesh will be employed in the region adjacent to the droplet, while a coarser mesh will be used in regions farther away from the droplet. Specifically, a uniform mesh resolution of 0.115 mm will be applied within the shadowed cuboid box region, which matches the parameters used in the two-dimensional case. This resolution corresponds to approximately 434 cells to effectively capture the characteristics of the spherical droplet. This region will contain about 2.1×10^8 mesh cells to comprehensively cover the typical development area of the droplet shell.

Beyond this region, the mesh resolution will become progressively coarser at a ratio of 1.1. All other conditions will be consistent with those used in the two-dimensional simulations, with the adoption of symmetry boundary conditions for two surfaces connected to the droplet.

It is worth noting that the computational configuration used in this study surpasses that of previous simulations involving water droplets, such as the work by Meng and Colonius [33], where they used WENO3 and a grid resolution equivalent to 100 cells per original droplet diameter. In the following section, we will delve into the deformation of the two-phase interfaces and the development of vortices, considering the three-dimensional characteristics of the interaction.

1. Evolution of surface deformation

Simulating two-phase interfaces often results in a smeared interface spanning several grid cells, as observed in our study and others [33]. This is because the chosen method inherently averages properties across a small region. The accuracy of the interface visualization can be further affected by the specific value chosen for the isosurface or isopleth (which represent surfaces or lines of constant value).

In our postprocessing, we distinguish between liquid and gas phases using the mass fraction of the gas phase and employ isosurfaces ranging from 0.01 to 0.99 to represent the two-phase interface. These isosurfaces account for the inherent uncertainty in the postprocessing stage due to the smeared interface characteristics [refer to Figs. 17(f)–17(h) and the Supplemental Material [95] for examples). As noted in Ref. [33], the choice of gas mass fraction value can influence the observed interface structures.

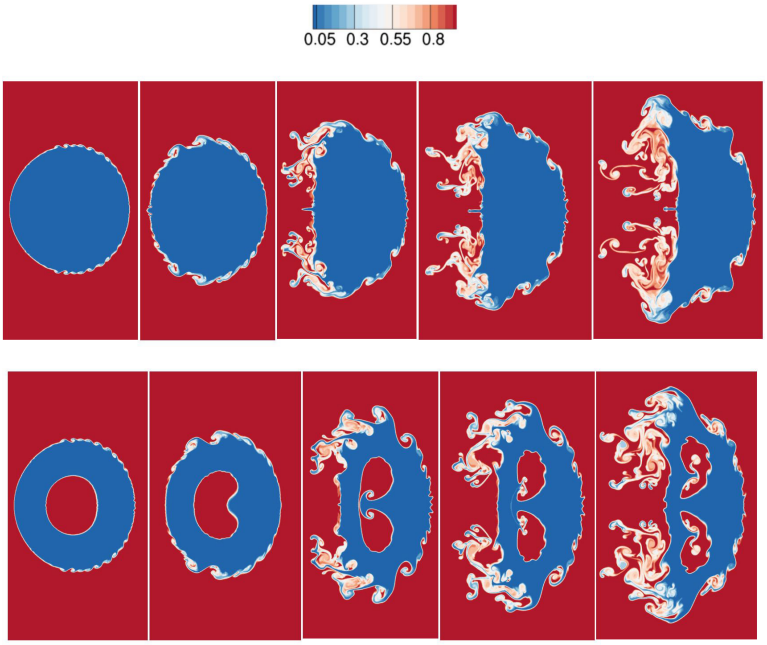

(a) Pure cylinder: upper; the cylinder embedded with a cavity: lower.

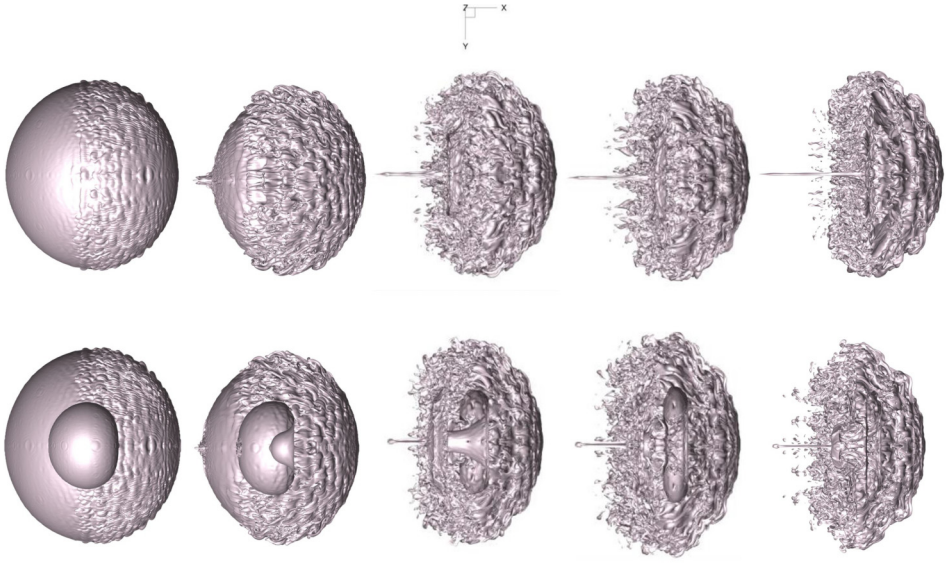

(b) Pure droplet: upper; droplet shell: lower.

FIG. 17. (a) Gas mass fraction contour of the cylinder case at $t^* = 15$, 27, 49, 56, and 66 (from left to right). [(b)–(e)] Isosurface of the gas mass fraction 0.5 of the droplet case at $t^* = 15$, 27, 49, 56, and 66 (from left to right). (f) Isosurfaces of the gas mass fraction, 0.01, 0.05, 0.25, 0.5, 0.75, 0.95, and 0.99 (from left to right) at $t^* = 27$. (g) Isosurfaces of the gas mass fraction, 0.01, 0.05, 0.25, 0.5, 0.75, 0.95, and 0.99 (from left to right) at $t^* = 49$. (h) Isosurfaces of the gas mass fraction, 0.01, 0.05, 0.25, 0.5, 0.75, 0.95, and 0.99 (from left to right) at $t^* = 56$.

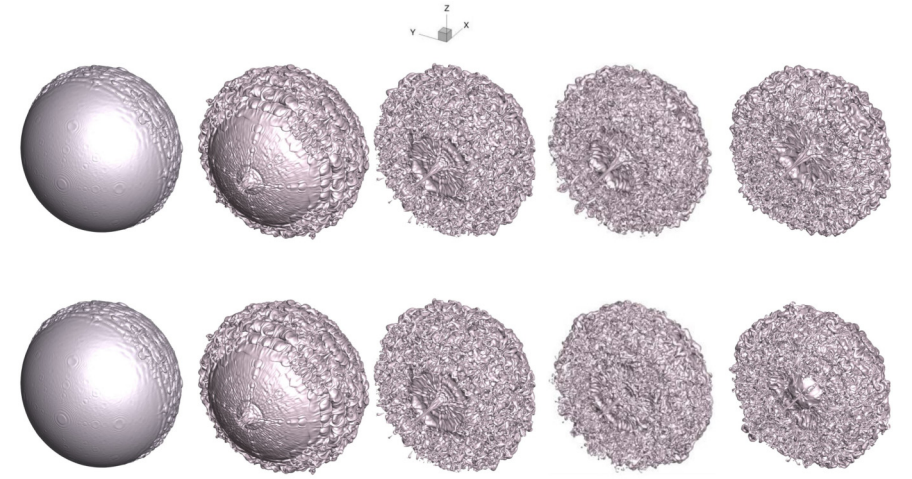

(c) Pure droplet: upper; droplet shell: lower.

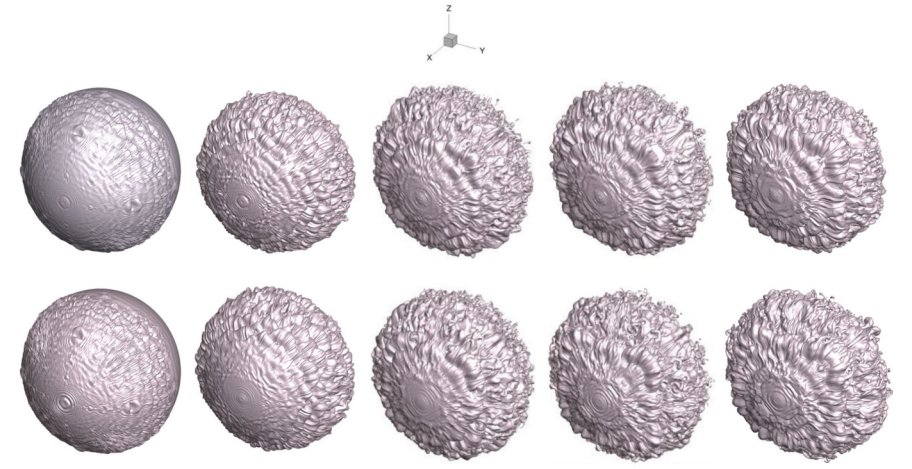

(d) Pure droplet: upper; droplet shell: lower.

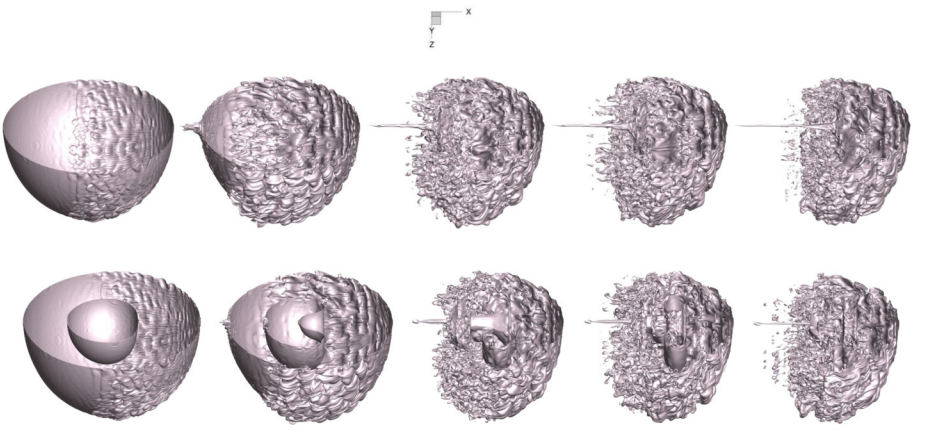

(e) Pure droplet: upper; droplet shell: lower.

FIG. 17. (*Continued*).

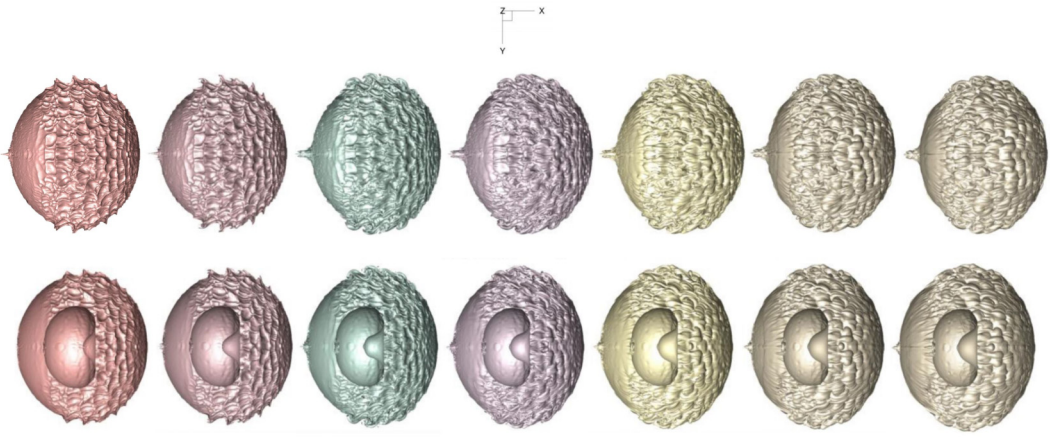

(f) Pure droplet: upper; droplet shell: lower.

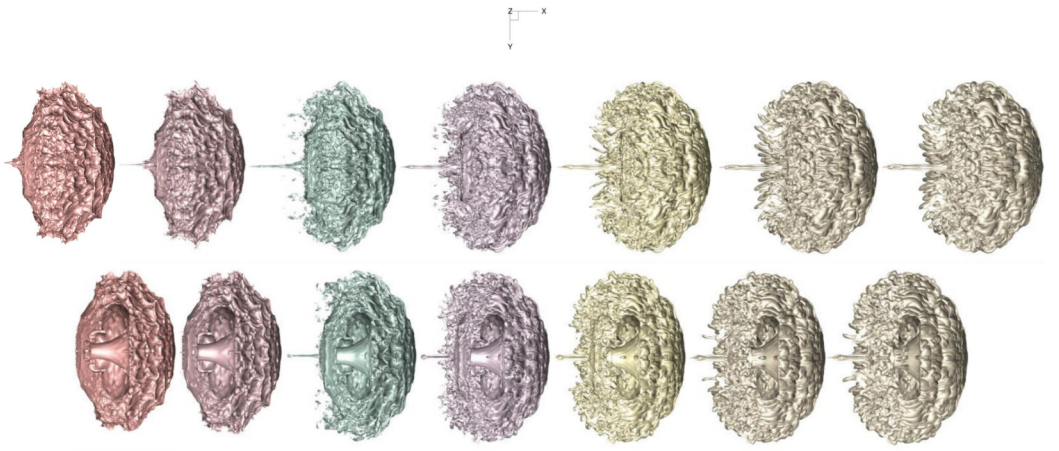

(g) Pure droplet: upper; droplet shell: lower.

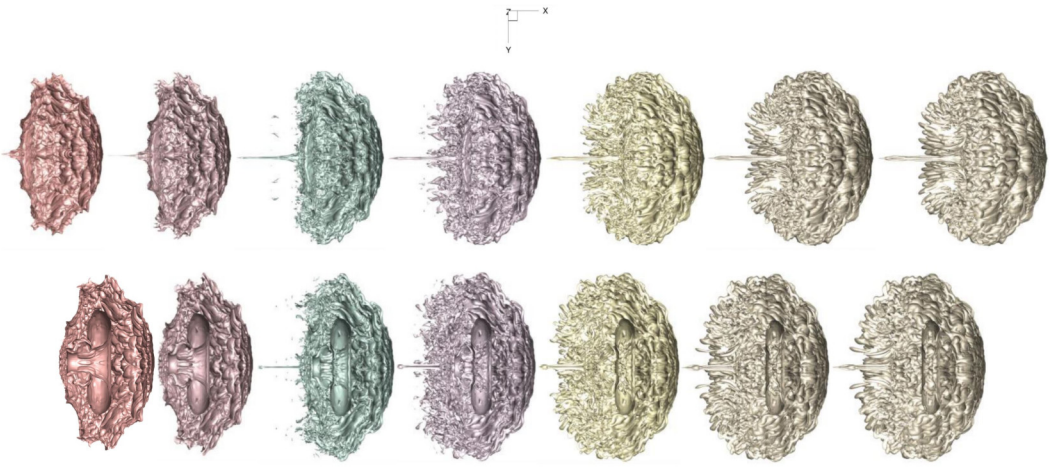

(h) Pure droplet: upper; droplet shell: lower.

FIG. 17. (*Continued*).

It is important to remember that these three-dimensional structures are only visualized for a specific isosurface value (e.g., 0.5 for gas mass fraction). This approach aligns with the postprocessing technique used in Ref. [33], where varying gas fraction values for isosurfaces resulted in the visualization of different droplet breakup structures. Unfortunately, there is no perfect choice for the isosurface value, as the numerical method itself introduces uncertainty that cannot be entirely eliminated. In essence, the chosen value (mass or volume fraction) to define the interface affects the shapes and structures captured by the isosurfaces.

Similar to the work in Ref. [33], we acknowledge the presence of smeared or diffuse features in our visualization, even with our resolution of 434 cells per initial diameter to represent the droplet. Nevertheless, based on our grid convergence study and the chosen numerical scheme, we are confident that the dominant structures and key features are accurately captured. While the numerical scheme might lead to the appearance of smaller breakups, these phenomena cannot be validated against experimental data and are likely artifacts of the simulation. It is important to emphasize that the overall conclusions are not affected by the isosurface value selection, as we consistently apply the same analytical and quantitative methods throughout all cases. Considering the numerical methods employed and the achieved mesh independence with 434 grids per diameter, the results provide a reasonable representation of the physical phenomena, with the understanding that the smeared region incorporates the effects of numerical viscosity.

The results depicted in Fig. 17 illustrate the progression of deformed two-phase contact structures for both the cylinder case and the three-dimensional droplet case simulations. A threshold value of 0.5 is employed for the isosurface to delineate the gas phase for the three-dimensional droplet case. Various distinctive deformation scenarios that capture the dynamics of the droplet structure have been chosen for analysis. The qualitative descriptions provided in two-dimensional simulations, as discussed in Secs. III A 1 and III A 2, are equally applicable to the three-dimensional simulations, with the primary distinction being the added dimension. In comparison to the two-dimensional findings, the deformation processes remain quite analogous, yet the inclusion of the third dimension allows for a more comprehensive representation of the dynamics. The structures observed in these simulations, including sheets, petal-shaped structures or lobes, and ligaments, exhibit pronounced three-dimensional characteristics that were not discernible in the two-dimensional simulations.

Combining the insights from Secs. III A 2 and III B 1, we can draw the following conclusions: The droplet effectively behaves like a solid block, contributing to the formation of a plume shape characterized by a flattened disk or a cupcakelike structure. Within the recirculation region, counter-rotating vortices develop near the leeward side of the droplet, playing a crucial role in shaping this distinctive form and drawing liquid sheets from both the droplet's equator and its flattened rear [33]. The presence of an enclosed cavity attached to the downstream side of the deforming droplet is associated with the development of a recirculation region that entrains fluid and redirects it upstream to impact the leeward side of the droplet. The continual deformation of the droplet in the normal direction increases its projected area for aerodynamic effects, further promoting the flattening of the liquid droplet and assisting in its breakup [49]. Additionally, as shown in Fig. 17(e), the internal cavity serves to reduce jet formation. Notably, the internal spherical cavity undergoes deformation, transforming into a kidney-shaped structure before breaking into a toroidal shape.

Surface tension is typically disregarded in transcritical flows [10,51,52,71–76] because the surface tension coefficient significantly diminishes in the vicinity of the critical point. In references related to simulation at near-critical conditions [51,52], the Weber number is defined as $\mathrm{We} = \rho_{\mathrm{post}} u_{\mathrm{post}}^2 D_0/\sigma$, which is adopted to assess the type of deformation. For the current case with a Mach number of 1.2, with $T_{\mathrm{ref}} = 650$ K, $p_{\mathrm{ref}} = 6$ MPa, $u_{\mathrm{post}} = -160.3$ m/s, $D_0 = 50$ mm, and $\rho_{\mathrm{post}} = 40.38$ kg/m^3, assuming that $\sigma = 0.001$ N/m [51], then the approximate Weber number is about 5×10^7. It is therefore reasonable to assume that, during the initial phase of development, there should be no discernible difference between the flow simulated with or without surface tension. Consequently, it is anticipated that these cases with a very large Weber number [96] will fall into the regime of shear-induced entrainment (SIE) breakup. However, neglecting surface tension in

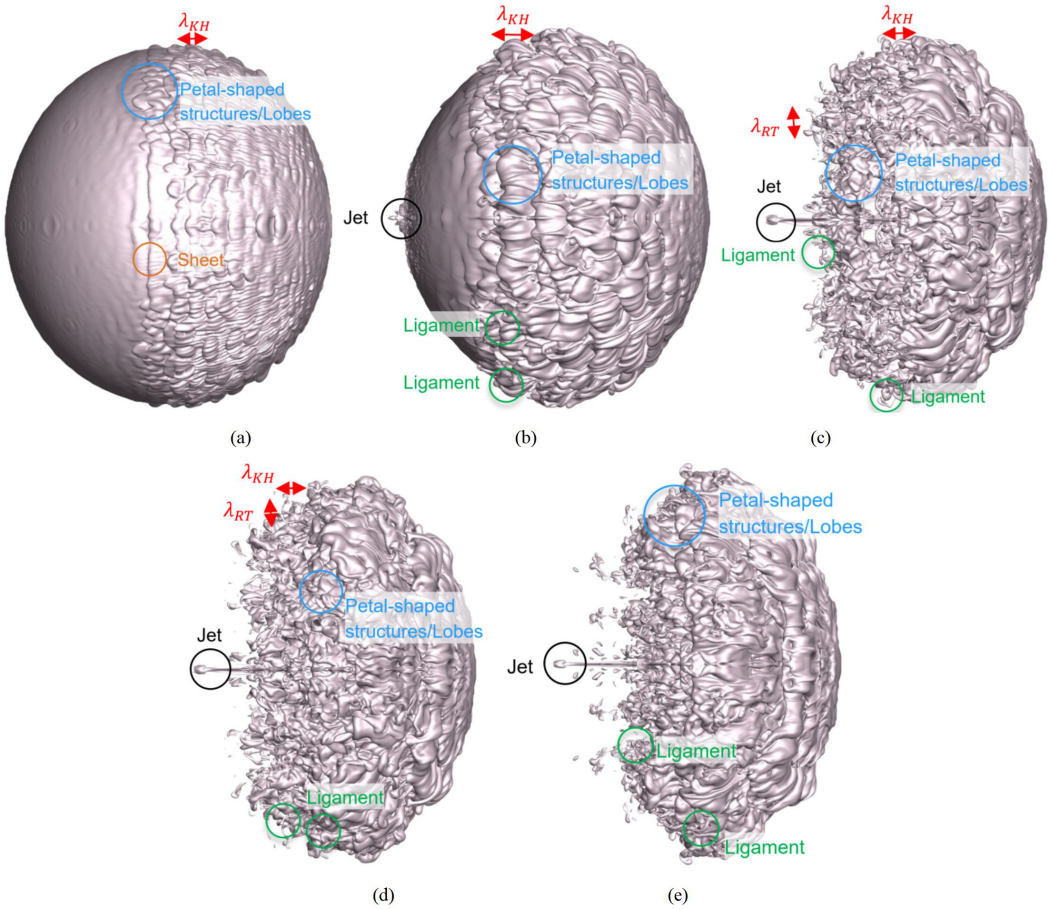

FIG. 18. Isosurface of the gas mass fraction 0.5 of the droplet with gas cavity at $t^* =$ (a) 15, (b) 27, (c) 49, (d) 56, and (e) 66.

the model simplifies the problem by replacing the actual phase interface with a contact region. While both fluids are initially separated in this region, they can mix during the deformation process. Strictly speaking, neglecting surface tension means simulating contact region deformation rather than interface breakup, although the established terminology in the field seems to differ.

In the initial stages, spanning from $t^* = 0$ to $t^* = 27$, the RMI induces morphological deformations of the two-phase structures, causing lobes to stretch and ligaments to form. In the later stages, occurring between $t^* = 49$ and $t^* = 66$, the deformation of ligaments becomes apparent, especially when visualized using an isosurface value of a mass fraction of 0.5.

The numerical results capture the key characteristics of inertia-driven mechanisms, although neglecting surface tension inherently leads to a loss of sharp interfaces. Despite satisfying the SIE breakup condition and capturing the expected phenomena, the results are limited by their numerical nature and dependence on a specific isosurface value selection. These limitations (surface tension neglect and finite resolution) confine the interpretation of the simulated structures as analogies, albeit reasonable ones based on the dominant forces.

In Fig. 18, we observe the formation of internal jets, deformation of the internal bubble, and its eventual transformation into a toroidal shape. Notably, the emergence of external jets on the downstream side of droplet (DSD) is suppressed in cases involving a gas cavity.

Our analyses are based on analogies and further confirmation will require experimental data. It should be noted that numerous mechanisms contribute to the disintegration process, an area explored in prior studies [49,97–103] yet still evolving. SIE breakup involves the formation of sheets, petal-shaped structures or lobes, and ligaments. This process is closely linked to the development of Kelvin-Helmholtz (KH) waves and flow entrainment, particularly on the windward side of the droplet, as well as liquid transport [49] due to droplet deformation, especially on the leeward side.

KH waves primarily form on the droplet's surface between the front to the peak (FTP) and the equator, where shear effects are predominant [97]. These waves can induce droplet stripping, resulting in KH-based liquid transport mechanisms [49,97,98] [see Fig. 18(a)]. As observed in Figs. 18(a)–18(c) and Sec. III A 2, KH waves gradually increase in amplitude and then deflect in the streamwise direction when becoming entrained by the external airflow. The entrainment of the flow causes the surface waves to move downstream [49], leading to the accumulation of liquid as sheets, petal-like structures, or lobes. The development of these surface structures is influenced by the entrainment force induced by the external airflow and by the driving force of the internal flow due to the KH wave. Additionally, shock-induced internal flow with vortices can contribute to the rupture of surface structures [99].

Moreover, petal-like structures or lobes undergo a cascade process [49] during the formation of ligaments, including the stretching of the structures, corrugation stretching, and the perforation of holes that lead to bridge breakup [100,101]. The formation of holes can result in the rupture of sheet and petal-like structures, ultimately yielding cylindrical ligaments. These holes can increase in size over time. In cases where surface tension dominates, these formed ligaments can undergo further secondary atomization into smaller droplets via Rayleigh-Plateau instability (RPI). However, for fluids at near-critical conditions with a relatively higher gas-liquid density ratio and high kinetic energy, surface tension effects are negligible [52] for relatively large ligaments. It should be noted that our simulation's resolution cannot capture the minuscule effects of surface tension, particularly given the chosen method's limitations in representing infinitely sharp boundaries.

Furthermore, Liang *et al.* [58] conducted an experiment on the interaction between a planar shock wave and a water droplet containing a vapor cavity under subcritical conditions. In our cases, under near-critical conditions (our Fig. 17), the ringlike structures, the transverse jets are similar to their experimental data under subcritical conditions (their Fig. 2). In this way, the deformation of our near-critical droplet behaves similarly to a water droplet in air under subcritical conditions [58].

We also analyze the drift of the center-of-mass velocity for these selected times. The results from the two-dimensional simulation are used for comparison, as shown in Fig. 19. When comparing the results between two-dimensional and three-dimensional simulations, it becomes evident that there are significant differences, highlighting the importance of three-dimensional simulations for more realistic and quantitatively accurate descriptions. The presence of a gas cavity enhances the drift velocity in both cases. While two-dimensional studies offer qualitative insights into the effects of a cavity on the droplet evolution process, three-dimensional studies provide more detailed information on deformation and interactions.

2. Vorticity evolution and vortical structures

Figure 20 shows the contour of Z vorticity of the plane $Z = 0$, and Y vorticity of the plane $Y = 0$. Figures 21 and 22 show the isosurface of $\Omega = 0.52$. $\Omega = ||B||^2/(||B||^2 + ||A||^2 + \varepsilon)$, where, ε is a minor value to prevent division by zero, $||B|| = 0.5((\partial u/\partial y - \partial v/\partial x)^2 + (\partial u/\partial z - \partial w/\partial x)^2 + (\partial v/\partial z - \partial w/\partial y)^2)$, and $||A|| = (\partial u/\partial x)^2 + (\partial v/\partial y)^2 + (\partial w/\partial z)^2 + 0.5(\partial u/\partial y + \partial v/\partial x)^2 + 0.5(\partial u/\partial z + \partial w/\partial x)^2 + 0.5(\partial v/\partial z + \partial w/\partial y)^2$.

The results presented in Figs. 20–22 demonstrate the gradual development of vortex structures after the shock interacts with the two-phase interface. The following key observations can be made:

Early vorticity induction. In the initial stages, vorticity is induced on the outer surface of the droplet due to baroclinic effects (baroclinic vorticity). Near the upstream surface of the droplet (USD), most vortices are oriented perpendicular to the flow direction [Figs. 21(a) and 22(a)].

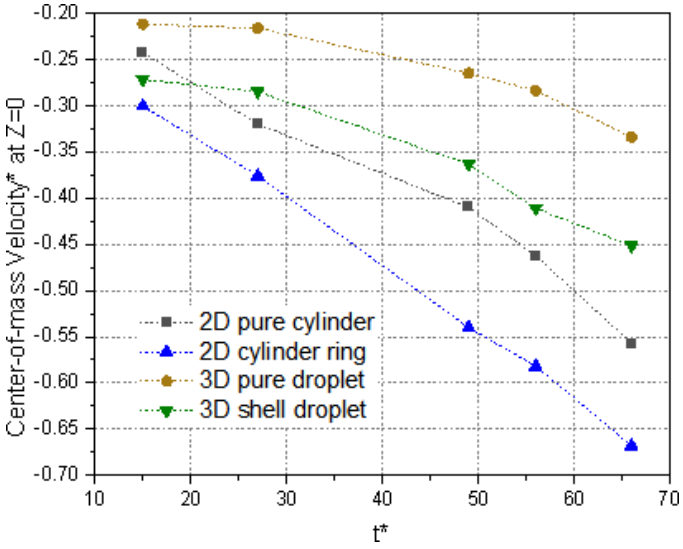

FIG. 19. The drift of the center-of-mass position and velocity (dimensionless at 100 m/s).

Streamwise-type vortices. As the simulation progresses, additional vortices are generated near the USD. Notably, most of the newly formed vortex filaments near the downstream surface of the droplet (DSD) are parallel to the flow direction [Fig. 21(b)]. These streamwise-type vortices exhibit elongated hairpinlike structures in the azimuthal direction of the vortex core [Figs. 21(c)–21(e) and 22(c)–22(e)].

Vortex stretching and mixing. Fine filaments of vorticity serve as indicators of areas with intense vortex stretching. Much like the discussion in Sec. III B 1, the heightened vorticity fosters the mixing of fluids and amplifies the process of transferring and dissipating vortex energy. In the later stages, the progression of Richtmyer-Meshkov instability (RMI), Rayleigh-Taylor instability (RTI), and Kelvin-Helmholtz instability (KHI) further contributes to the deformation of the shocked droplet and augments its mixing properties, as illustrated in Figs. 21(e) and 22(e).

Azimuthal instability. The azimuthal instability of the axisymmetric KH waves can be caused by baroclinic effects (associated with RMI or RTI) and the generation of streamwise vortices [49]. This leads to the formation of petal-like structures or lobes.

Baroclinic effects and vortex strain. At low gas-liquid density ratios, the baroclinic effects are significant due to the high-density gradient across the interface. As the density ratio increases, vortex-strain interactions (due to the vortex tilting and stretching mechanism) become more important in azimuthal modulation on KH waves due to higher gas inertia [100–103]. This results in a higher vortex strain near the liquid interface, and the contribution of the baroclinic effect to the generation of streamwise vorticity is reduced.

Roll-up vortex structures. When we combine the findings from Fig. 17, which pertains to the region near ligament formation and deformation, with the insights from Fig. 18, we observe a profusion of roll-up vortex structures, particularly streamwise vortices, as depicted in Fig. 21. These streamwise vortices exhibit a pair of positive and negative values, as shown in Fig. 20, and play a pivotal role in influencing the dynamic behavior of the system.

Such vortex structures and behavior of the droplet with a cavity represent an observation at near-critical conditions. The complex interplay of various vorticity mechanisms, baroclinic effects, and instabilities contributes to the intricate dynamics observed in the simulations.

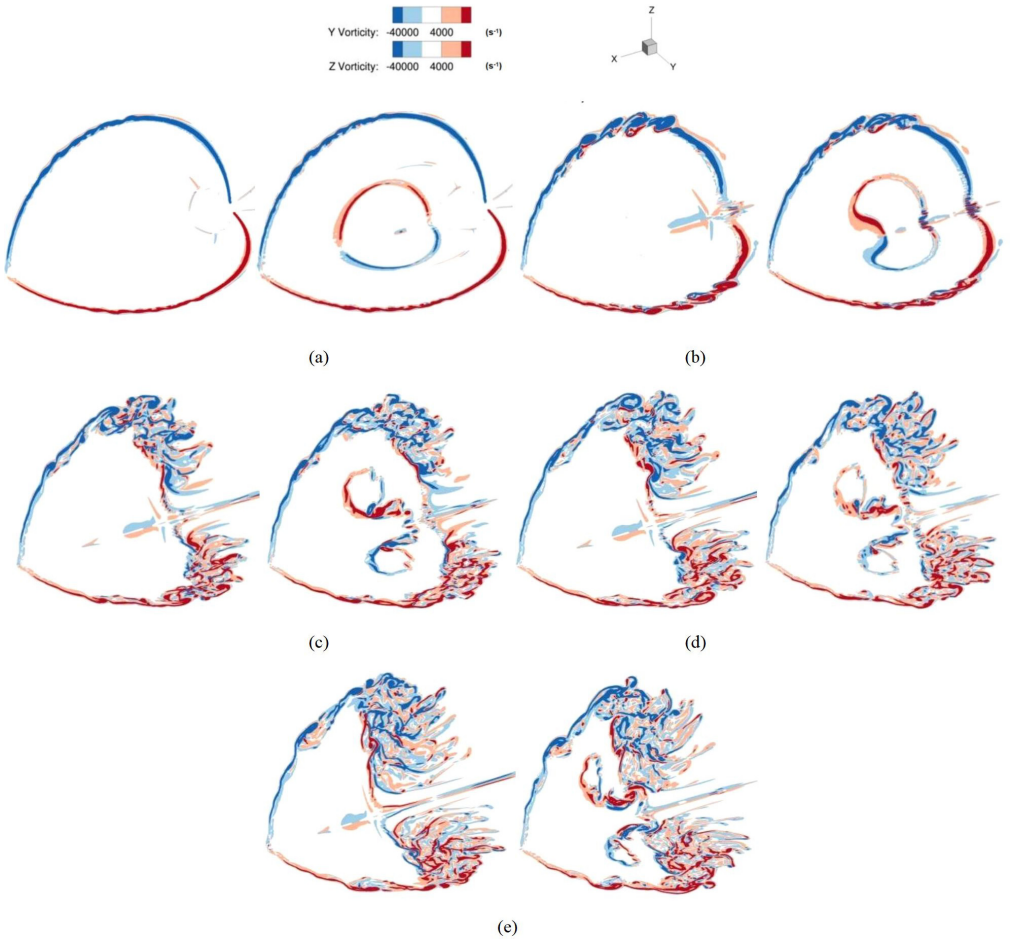

FIG. 20. The contour of Z vorticity of the plane $Z = 0$, and Y vorticity of the plane $Y = 0$ at $t^* =$ (a) 15, (b) 27, (c) 49, (d) 56, and (e) 66.

IV. CONCLUSIONS

This study examines the intricate interactions of shock waves with a cylinder or droplet containing an embedded gas cavity, particularly under near-critical thermodynamic conditions. The gas-cavity presence significantly impacts various properties of the cylinder or droplet, encompassing flow wave patterns, morphological changes, vortex formation, enstrophy, and three-dimensional developmental characteristics. For processes at a near-critical conditions, we come to the following observations.

(1) Distinct wave patterns and morphology changes: The presence of an internal gas cavity significantly alters the observed wave patterns and interactions. A detailed analysis of various parameters, including cylinder and internal bubble morphological changes, provides valuable insights into shock-induced deformation and wave interactions. We examined the interaction in detail, focusing on the early and late stages such as shock impingement, wave evolution, and morphological deformation. The internal structures observed resemble those reported in numerical and experimental studies of shocked light bubbles. Interestingly, while the wave patterns at near-critical conditions are similar to those obtained in the case with the cylinder consisting of SF_6 in air at subcritical

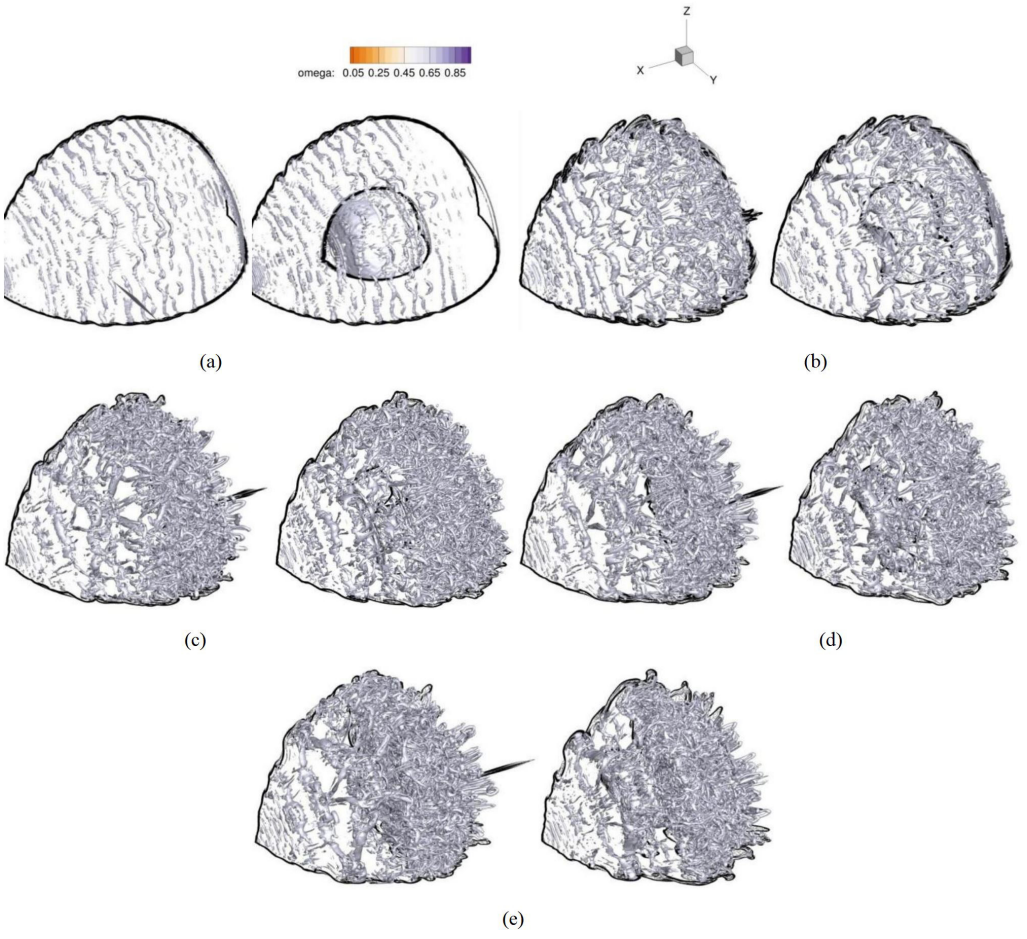

FIG. 21. Isosurface of $\Omega = 0.65$ at $t^* =$ (a) 15, (b) 27, (c) 49, (d) 56, and (e) 66.

conditions, the deformation behavior of the current cylinder under near-critical conditions is more akin to that of a water column in air under subcritical conditions.

(2) Vortex formation and baroclinic effects: The simulations demonstrate the emergence of vortices and the deposition of vorticity on the surfaces of the cylinder or droplet. Vortices develop on the external surfaces, and the presence of the gas cavity has a notable impact on the creation of liquid mushroom jets, vortex structures, and the rupture of the cavity bubble, all of which contribute to the deformation of the interface.

(3) Enstrophy and mixing: Enstrophy, reflecting the mixing process, evolves over time. The presence of the gas cavity results in increased enstrophy due to internal jet formation and distortion of the mushroom structure. The generation of baroclinic vorticity intensifies enstrophy, promoting liquid-gas mixing.

(4) Center-of-mass redistribution: The analysis includes the drift of the center-of-mass position and velocity. The presence of the gas cavity enhances the shift velocity in both cylinder and droplet cases.

(5) Three-dimensional interface deformation: Three-dimensional simulations are crucial for revealing complex, deformed structures near the two-phase interface, such as ligaments, lobes, petal

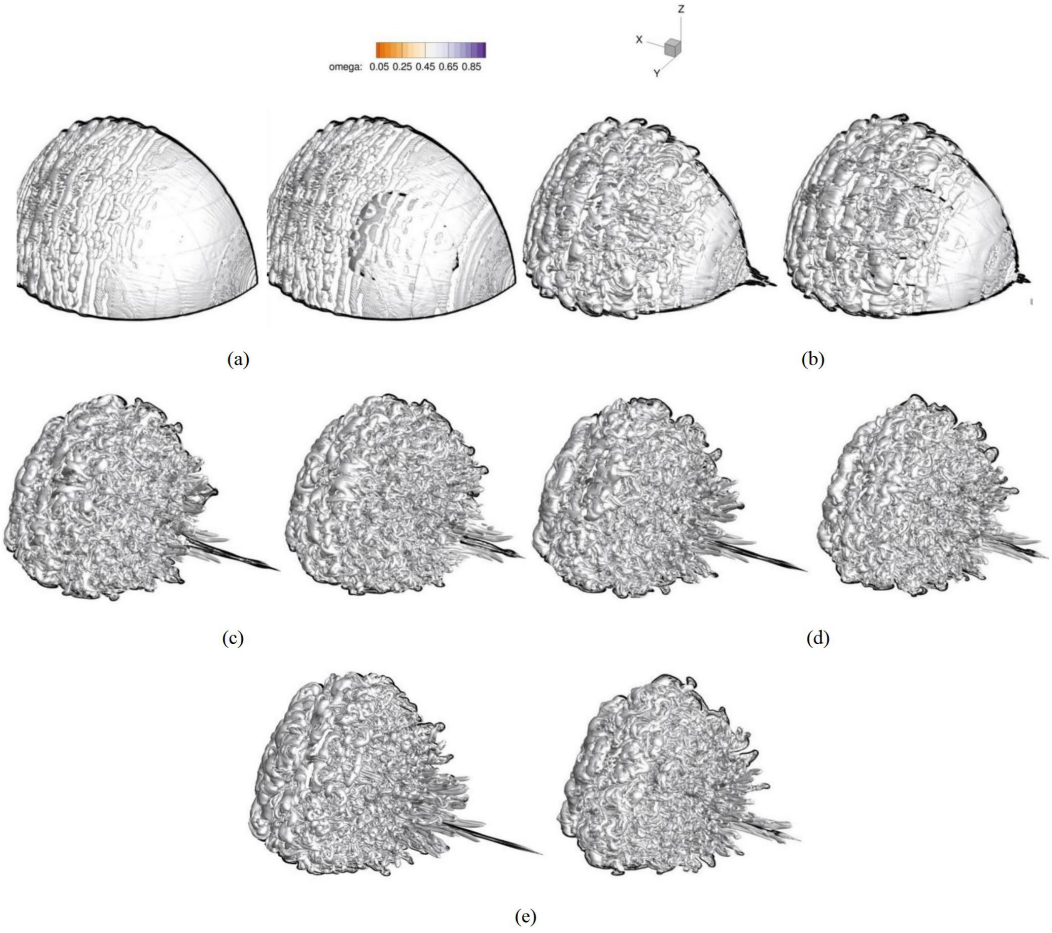

FIG. 22. Isosurface of $\Omega = 0.52$ at $t^* =$ (a) 15, (b) 27, (c) 49, (d) 56, and (e) 66.

shapes, and toroidal structures. These features, along with the three-dimensional vorticity distribution, cannot be captured by two-dimensional simulations. A comparative analysis is conducted to examine the similarities and differences between the cases involving droplets and the cylindrical column. Interestingly, the deformation of the droplet shell at near-critical conditions resembles that of a water droplet containing a cavity in air under subcritical conditions, exhibiting similar ringlike structures and the transverse jet. While our simulations are comparable to the characteristics of shear-induced entrainment for a chosen mass fraction, a complete understanding of the underlying physics requires further experimental validation.

Future work should encompass additional simulations with varying parameters alongside more extensive experimental research. This comprehensive approach will enable a deeper understanding of the complex mechanisms governing these interactions and disintegration processes.

ACKNOWLEDGMENT

The authors gratefully acknowledge the Leibniz Supercomputing Centre for funding this research by providing computing time on its Linux-Cluster.

APPENDIX A: DETAILS OF THE PENG-ROBINSON EOS

Here

$$p = \frac{RT}{v-b} - \frac{a}{v^2+2bv-b^2}, \tag{A1}$$

where T is the temperature, R is the universal gas constant, v is the molar volume, $v = M/\rho$, and M is the molar mass. Coefficients are $a = \sum_{\alpha=1}^{N}\sum_{\beta=1}^{N} X_\alpha X_\beta a_{\alpha\beta}$ and $b = \sum_{\alpha=1}^{N} X_\alpha b_\alpha$.

Specifically, X_α is the mole fraction of species α and in-total species number is N; coefficients $a_{\alpha\beta} = 0.457236(RT_{c,\alpha\beta})^2/p_{c,\alpha\beta}(1+c_{\alpha\beta}(1-\sqrt{T}/T_{c,\alpha\beta}))^2$ and $b_\alpha = 0.077796RT_{c,\alpha}/p_{c,\alpha}$ are obtained according to the mixing rules [104]. $p_{c,\alpha\beta}$ is the critical mixture pressure and $p_{c,\alpha\beta} = Z_{c,\alpha\beta}RT_{c,\alpha\beta}/v_{c,\alpha\beta}$, $c_{\alpha\beta} = 0.37464 + 1.5422\omega_{\alpha\beta} - 0.26992\omega_{\alpha\beta}^2$, $T_{c,\alpha\beta}$ is the critical mixture temperature, and $T_{c,\alpha\beta} = \sqrt{T_{c,\alpha}T_{c,\beta}}(1-k_{\alpha\beta})$. $T_{c,\alpha}$ and $T_{c,\beta}$ are critical temperatures for species α and β, and $k_{\alpha\beta}$ is the binary interaction parameter.

The critical mixture molar volume $v_{c,\alpha\beta}$, the critical mixture compressibility $Z_{c,\alpha\beta}$, and the acentric factor $\omega_{\alpha\beta}$ are denoted as $v_{c,\alpha\beta} = (1/8)(v_{c,\alpha}^{1/3} + v_{c,\beta}^{1/3})^3$, $Z_{c,\alpha\beta} = (1/2)(Z_{c,\alpha} + Z_{c,\beta})$, and $\omega_{\alpha\beta} = (1/2)(\omega_\alpha + \omega_\beta)$, where $v_{c,\alpha}^{1/3}$ and $v_{c,\beta}^{1/3}$ are critical molar volumes for species α and β, $Z_{c,\alpha}$ and $Z_{c,\beta}$ are critical compressibility factors for species α and β, and ω_α and ω_β are acentric factors for species α and β. Further details can be found in Refs. [17,104].

APPENDIX B: SOLUTION OF THE CUBIC EQUATION

When solving cubic equations of state (EOS), such as the PR-EOS, it is important to recognize that there may be three roots. However, it is essential to disregard nonphysical roots, which include negative values and complex values, and focus on identifying the real, positive roots [105–107]. The process of solving the cubic equation is outlined as follows:

$$x^3 + Ax^2 + Bx + C = 0, \tag{B1}$$

where A, B, and C are known coefficients obtained directly from the cubic EOS. The discriminant is $\Delta = D^2 + E^2$ and $D = (A/3)^3 - AB/6 + C/2$, $E = B/3 - (A/3)^2$.

For $\Delta = 0$, there are at least two equal roots, which are given by

$$x_1 = 2\sqrt[3]{-D} - \frac{A}{3}, \quad x_2 = x_3 = -\sqrt[3]{-D} - \frac{A}{3}. \tag{B2}$$

$\Delta > 0$, there are two nonphysical conjugate roots and one real root, $F = \sqrt[3]{-D+\sqrt{\Delta}}$, $G = \sqrt[3]{-D-\sqrt{\Delta}}$

$$\begin{aligned} x_1 &= F + G - \frac{A}{3}, \quad x_2 = -\left[\frac{1}{2}(F+G) + \frac{A}{3}\right] + \frac{\sqrt{3}}{2}(F-G)i, \\ x_3 &= -\left[\frac{1}{2}(F+G) + \frac{A}{3}\right] - \frac{\sqrt{3}}{2}(F-G)i. \end{aligned} \tag{B3}$$

$\Delta < 0$, there are three real and unequal roots, $\theta(\text{rad}) = \arccos(-D/\sqrt{-E^3})$,

$$\begin{aligned} x_1 &= 2\sqrt{-E}\cos\left(\frac{\theta}{3}\right) - \frac{A}{3}, \\ x_2 &= 2\sqrt{-E}\cos\left(\frac{\theta}{3} + \frac{2}{3}\pi\right) - \frac{A}{3}, \\ x_3 &= 2\sqrt{-E}\cos\left(\frac{\theta}{3} + \frac{4}{3}\pi\right) - \frac{A}{3}. \end{aligned} \tag{B4}$$

APPENDIX C: MODIFIED PR-EOS

The modified PR-EOS is designed to represent the saturation line in a straightforward manner. Within the vapor dome region, an approximate saturation pressure for the mixture is utilized. The algorithm for determining the pressure, which yields the temperature, density, and mass fraction, is as follows:

Step 1. Calculate the pressure from the PR-EOS giving the temperature and density, as well as the mass fraction. If nonpositive pressure ($p^* \leqslant 0$) is obtained from the relation $p^* = p_{\mathrm{PR-EOS}}(T, \rho, \xi_i)$, a small arbitrarily positive value such as 1 would be adopted to replace this nonpositive value ($p^* = 1\,\mathrm{Pa}$).

Step 2. Calculate the density from PR-EOS given the PR-EOS pressure p^*, temperature, and mass fraction, and check how many roots are obtained in the process $\rho^* = p_{\mathrm{PR-EOS}}(p^*, T, \xi_i)$.

Step 3.1. If there is only one real value for ρ^*, then the PR-EOS pressure p^* is chosen as the corrected pressure.

Step 3.2. If there is more than one root for (ρ^*), then the saturation pressure (p_{sat}) is given by calculating the root, $\partial p/\partial \rho = 0$, via PR-EOS. Generally, the one at the lower density value (ρ_{min}) would be selected from the two resulting roots. The saturation pressure (p_{sat}) is then defined as the pressure corresponding to this root (ρ_{min}).

Step 4. If the density that is given by the PR-EOS (lowest density root, $\rho^* = p_{\mathrm{PR-EOS}}(p^*, T, \xi_i)$) is very similar to the density provided (ρ), like $(\rho^* - \rho)/\rho < 10^{-4}$, then return the PR-EOS pressure p^*; otherwise, return the saturation pressure (p_{sat}).

In the case of DF methods or hybrid numerical schemes with a modified PR-EOS, it is crucial to calculate the temperature (T) for a given set of pressure (p), density (ρ), and mass fraction (ξ_i) using the modified PR-EOS ($T = p_{\mathrm{modified-PR-EOS}}(p, \rho, \xi_i)$). This can be expressed as follows:

Step 1. Initial guess (T_{guess}) temperature according to the initial condition and the temperature from the last time step.

Step 2. This T_{guess} is used to calculate the pressure, using modified PR-EOS $p_{\mathrm{guess}} = p_{\mathrm{modified-PR-EOS}}(T_{\mathrm{guess}}, \rho, \xi_i)$, where the state inside the vapor dome has already been corrected.

Step 3. If the pressure given by the modified PR-EOS ($p_{\mathrm{guess}} = p_{\mathrm{modified-PR-EOS}}(T_{\mathrm{guess}}, \rho, \xi_i)$) is very similar to the pressure given by the modified PR-EOS (p^*), e.g., $(p_{\mathrm{guess}} - p^*)/p^* < 10^{-6}$, then the temperature T_{guess} is selected as the correct temperature, $T = T_{\mathrm{guess}}$.

Step 4. Otherwise, the guess temperature is updated according to the secant method or gradient descent or Newton method, and the criteria are $p^* = p_{\mathrm{modified-PR-EOS}}(T_{\mathrm{guess}}, \rho, \xi_i)$ and $(p^* - p)/p < 10^{-6}$.

Step 5. The modified PR-EOS [71] also limits the speed of sound to a minimum value—the minimum speed of sound value used in this paper is 1 m/s [71]. Three subcritical isotherms of varying composition are depicted in Fig. 30 of Ref. [51] to showcase the modified PR-EOS.

APPENDIX D: EFFECTS OF COMPUTATIONAL DOMAIN AND BOUNDARY CONDITIONS ON NEAR-CRITICAL SHOCK-CYLINDER INTERACTIONS

Additional validations are presented in this section. These cases, when compared to previous validation cases, serve to elucidate the influence of the computational domain and boundary conditions on shock-cylinder interactions. As depicted in Fig. 23, reflective boundary conditions are employed within a constrained computational domain. The purpose of this comparison is to highlight the advancements offered by OWENO3 in contrast to the results obtained by the classical WENO3 method.

Due to its lower dissipation characteristics in comparison to the WENO3 scheme, the results obtained using the WENO3 scheme (Fig. 24) are outperformed by those of the OWENO3 scheme (Fig. 25) when employing the same mesh resolution. Irrespective of the mesh resolution chosen, the OWENO3 consistently delivers favorable results, whereas the performance of the WENO3

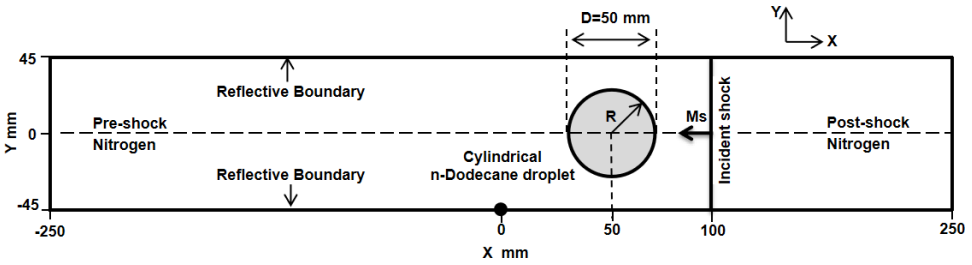

FIG. 23. The restricted computational domain of the shock-cylinder interaction at near-critical conditions (sketch map).

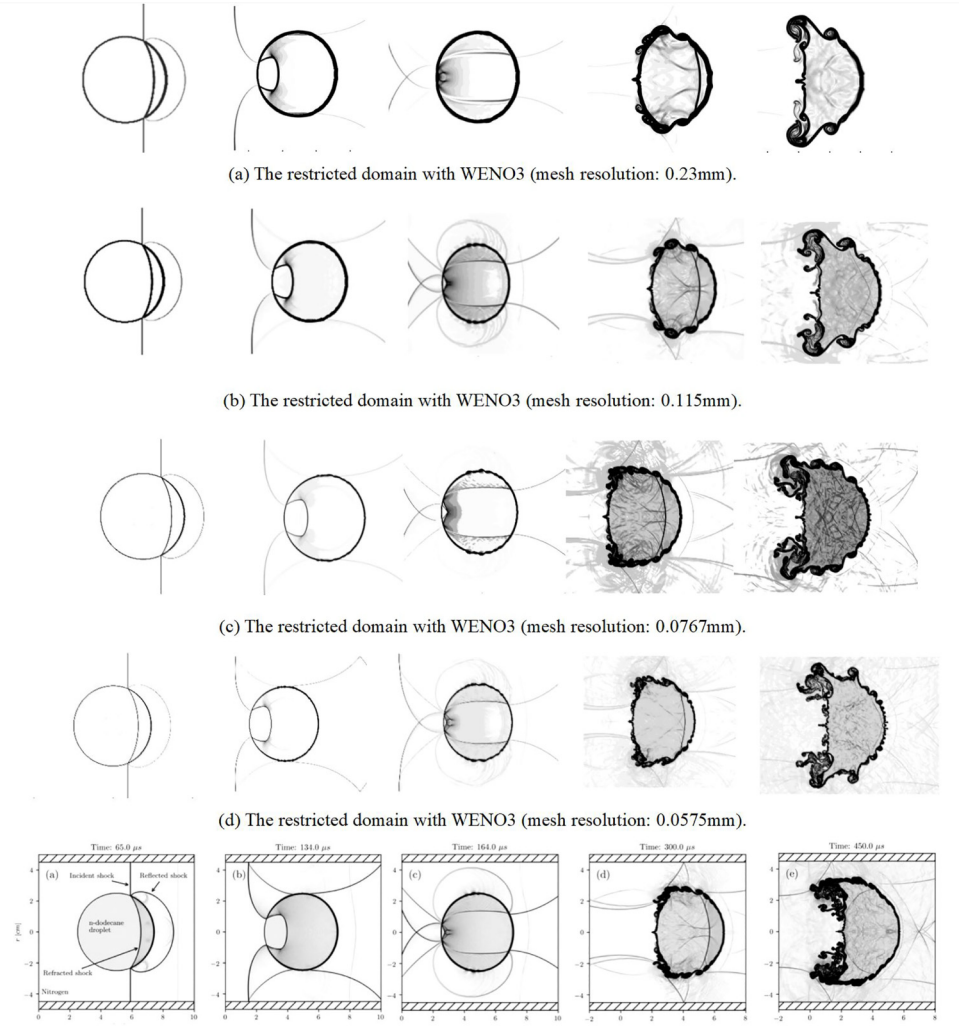

FIG. 24. The shock cylinder interaction within the restricted domain at times 65, 134, 164, 300, and 450 μs (from left to right). WENO3 with a mesh resolution of (a) 0.23 mm, (b) 0.115 mm, (c) 0.0767 mm, (d) 0.0575 mm. WENO5 with a mesh resolution of (e) 0.23 mm [51]. Reproduced from Ref. [51].

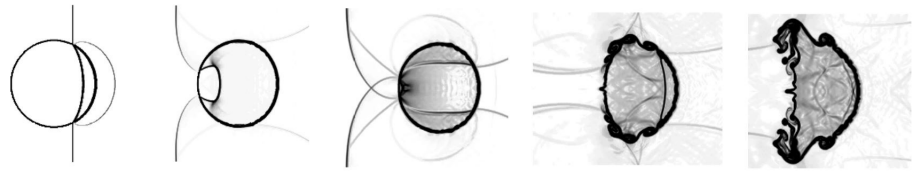

(a) The restricted domain with OWENO3 (mesh resolution: 0.23 mm).

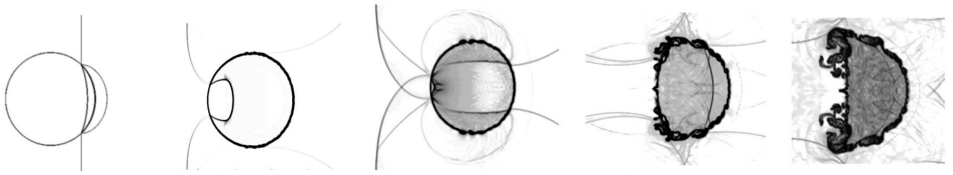

(b) The restricted domain with OWENO3 (mesh resolution: 0.115 mm).

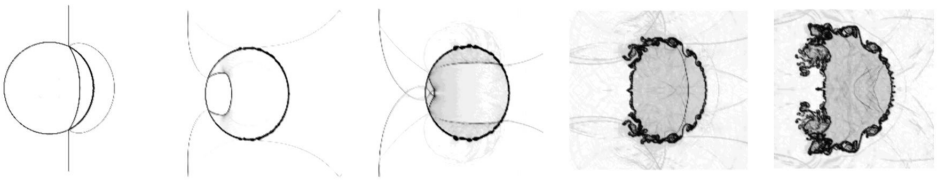

(c) The restricted domain with OWENO3 (mesh resolution: 0.0767 mm).

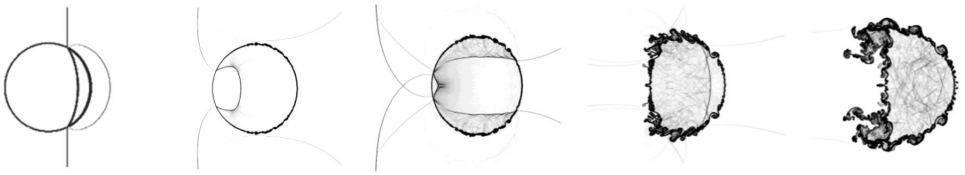

(d) The restricted domain with OWENO3 (mesh resolution: 0.0575 mm).

FIG. 25. The shock *n*-dodecane cylinder interaction within the restricted domain at times 65, 134, 164, 300, and 450 μs. OWENO3 with a mesh resolution of (a) 0.23 mm, (b) 0.115 mm, (c) 0.0767 mm, (d) 0.0575 mm.

scheme diminishes during later evolution times ($t = 450\,\mu s$) when using mesh resolutions of 0.23 or 0.115 mm.

Upon comparing results obtained from coarser mesh resolutions to finer ones across different numerical schemes, it can be deduced that the OWENO3 method, combined with a mesh resolution of 0.115 mm, can yield results comparable to those of the WENO5 scheme from Ref. [52], all while maintaining computational efficiency and accuracy.

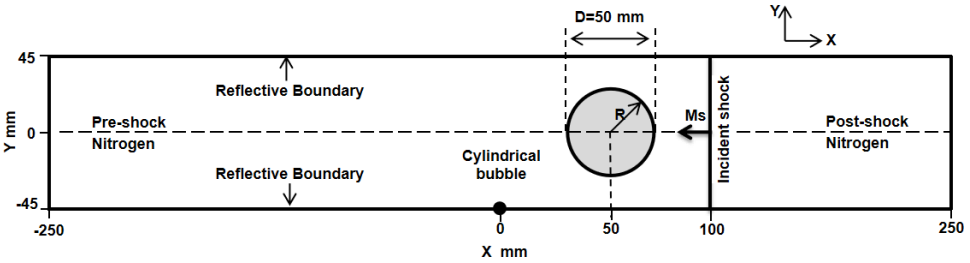

FIG. 26. Schematic of the shock-bubble interaction computational domain.

TABLE II. Initial conditions for the shock-bubble interaction.

Stage	p (Pa)	u (m/s)	v (m/s)	ρ (kg/m^3)	Non-dimension [108] (p, u, v, ρ)
Preshocked air	101325	0	0	1.225	(1,0,0,1)
Postshocked air	159059	113.5	0	1.686	(1.5698, −0.394, 0,1.3764)
Helium	101325	0	0	0.169	(1,0,0,0.138)

APPENDIX E: SHOCK INTERACTION WITH HELIUM BUBBLE

We have validated the current numerical scheme using the shock–helium bubble case as discussed in Refs. [22,108]. The computational domain is depicted in Fig. 26. The initial conditions are given in Table II.

We have employed a Cartesian mesh with a uniform resolution of 0.115 mm. The parameters for the NASA polynomials can be found in Ref. [78].

As depicted in Fig. 27, the results for the helium-air case exhibit excellent agreement with the findings presented by Quirk and Karni [22]. This alignment in results has also been observed by Haas and Sturtevant [21] and other researchers [109]. The methodology employed in this study effectively captures the underlying physical phenomena while ensuring robust performance. The selection of evolution time steps closely approximates the reference time, making minor deviations acceptable.

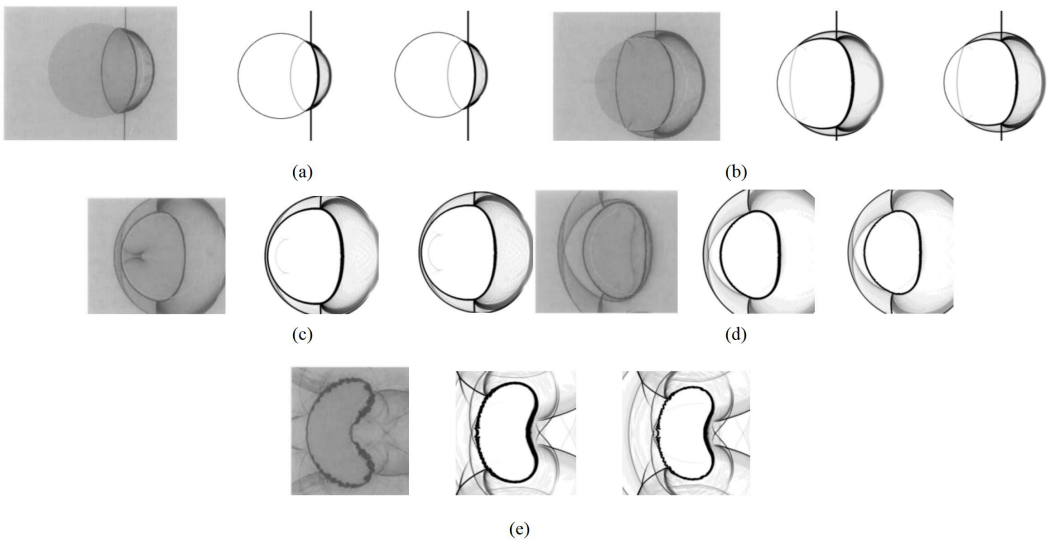

FIG. 27. Numerical schlieren images for the evolution of the shocked air-helium interaction at time (a) 32 μs, (b) 52 μs, (c) 72 μs, (d) 102 μs, and (e) 245 μs. The first column shows the current numerical results, while the others show the results from Ref. [22]. From left to right: numerical scheme (mesh resolution), reference scheme (0.056 mm), WENO3 (0.23 mm), and OWENO3 (0.23 mm). Reproduced from Ref. [22].

[1] Y. Zhou, Rayleigh-Taylor and Richtmyer-Meshkov instability induced flow, turbulence, and mixing. I, Phys. Rep. **720–722**, 1 (2017).
[2] Y. Zhou, Rayleigh-Taylor and Richtmyer-Meshkov instability induced flow, turbulence, and mixing. II, Phys. Rep. **723–725**, 1 (2017).
[3] M. Brouillette, The Richtmyer-Meshkov instability, Annu. Rev. Fluid Mech. **34**, 445 (2002).
[4] V. K. Tritschler, B. J. Olson, S. K. Lele, S. Hickel, X. Y. Hu, and N. A. Adams, On the Richtmyer-Meshkov instability evolving from a deterministic multimode planar interface, J. Fluid Mech. **755**, 429 (2014).
[5] R. D. Richtmyer, Taylor instability in shock acceleration of compressible fluids, Commun. Pure Appl. Math. **13**, 297 (1960).
[6] E. E. Meshkov, Instability of the interface of two gases accelerated by a shock wave, Fluid Dyn. **4**, 101 (1972).
[7] Z. Falgout, M. Rahm, D. Sedarsky, and M. Linne, Gas/fuel jet interfaces under high pressures and temperatures, Fuel **168**, 14 (2016).
[8] R. N. Dahms, J. Manin, L. M. Pickett, and J. C. Oefelein, Understanding high-pressure gas-liquid interface phenomena in diesel engines, Proc. Combust. Inst. **34**, 1667 (2013).
[9] R. N. Dahms, Understanding the breakdown of classic two-phase theory and spray atomization at enginerelevant conditions, Phys. Fluids **28**, 042108 (2016).
[10] J. Oefelein, G. Lacaze, R. Dahms, A. Ruiz, and A. Misdariis, Effects of real-fluid thermodynamics on high-pressure fuel injection processes, SAE Int. J. Engines **7**, 1125 (2014).
[11] P. C. Ma, Y. Lv, and M. Ihme, An entropy-stable hybrid scheme for simulations of transcritical real-fluid flows, J. Comput. Phys. **340**, 330 (2017).
[12] D. T. Banuti, M. Raju, and M. Ihme, *Supercritical pseudoboiling for general fluids and its application to injection*, Annual Research Briefs (2016), pp. 211–221.
[13] M. Oschwald, J. Smith, R. Branam, J. Hussong, A. Schik, B. Chehroudi, and D. Talley, Injection of fluids into supercritical environments, Combust. Sci. Technol. **178**, 49 (2006).
[14] W. O. H. Mayer, A. H. A. Schik, B. Vielle, C. Chauveau, I. Gokalp, D. G. Talley, and R. D. Woodward, Atomization and breakup of cryogenic propellants under high-pressure subcritical and supercritical conditions, J. Propul. Power **14**, 835 (1998).
[15] J. W. Chae, H. S. Yang, and W. S. Yoon, Supercritical droplet dynamics and emission in low speed cross-flows, J. Mech. Sci. Technol. **22**, 1586 (2008).
[16] V. Yang, Modeling of supercritical vaporization, mixing, and combustion processes in liquid-fueled propulsion systems, Proc. Combust. Inst. **28**, 925 (2000).
[17] V. Yang, N. Natan, and J.-S. Shuen, Vaporization of liquid oxygen (LOX) droplets in supercritical hydrogen environments, Combust. Sci. Technol. **97**, 247 (1994).
[18] V. Yang, G. C. Hsiao, J. S. Shuen, and K. C. Hsieh, Droplet behavior at supercritical conditions, Recent Adv. Spray Combust. **1**, 413 (1996).
[19] C. Crua, J. Manin, and L. M. Pickett, On the transcritical mixing of fuels at diesel engine conditions, Fuel **208**, 535 (2017).
[20] H. Meng, G. C. Hsiao, V. Yang, and J. S. Shuen, Transport and dynamics of liquid oxygen droplets in supercritical hydrogen streams, J. Fluid Mech. **527**, 115 (2005).
[21] J. F. Haas and B. Sturtevant, Interaction of weak shock waves with cylindrical and spherical gas inhomogeneities, J. Fluid Mech. **181**, 41 (1987).
[22] J. J. Quirk and S. Karni, On the dynamics of a shock-bubble interaction, J. Fluid Mech. **318**, 129 (1996).
[23] S. Kumar, G. Orlicz, C. Tomkins, C. Goodenough, K. Prestridge, P. Vorobieff, and R. Benjamin, Stretching of material lines in shock-accelerated gaseous flows, Phys. Fluids **17**, 082107 (2005).
[24] G. Layes, G. Jourdan, and L. Houas, Distortion of a spherical gaseous interface accelerated by a plane shock wave, Phys. Rev. Lett. **91**, 174502 (2003).
[25] G. Layes, G. Jourdan, and L. Houas, Experimental investigation of the shock wave interaction with a spherical gas inhomogeneity, Phys. Fluids **17**, 028103 (2005).
[26] G. Layes, G. Jourdan, and L. Houas, Experimental study on a plane shock wave accelerating a gas bubble, Phys. Fluids **21**, 074102 (2009).

[27] A. F. Nowakowski, A. Ballil, and F. C. G. A. Nicolleau, Passage of a shock wave through inhomogeneous media and its impact on gas-bubble deformation, Phys. Rev. E **92**, 023028 (2015).
[28] D. Ranjan, J. Oakley, and R. Bonazza, Shock-bubble interactions, Annu. Rev. Fluid Mech. **43**, 117 (2011).
[29] C. Tomkins, S. Kumar, G. Orlicz, and K. Prestridge, An experimental investigation of mixing mechanisms in shock accelerated flow, J. Fluid Mech. **611**, 131 (2008).
[30] C. Tomkins, K. Prestridge, P. Rightley, M. Marr-Lyon, P. Vorobieff, and R. Benjamin, A quantitative study of the interaction of two Richtmyer-Meshkov-unstable gas cylinders, Phys. Fluids **15**, 986 (2003).
[31] Y. Zhu, L. Yu, J. Pan, Z. Pan, and P. Zhang, Jet formation of SF_6 bubble induced by incident and reflected shock waves, Phys. Fluids **29**, 126105 (2017).
[32] N. Hoppe, J. M. Winter, S. Adami, and N. A. Adams, ALPACA-a level-set based sharp-interface multiresolution solver for conservation laws, Comput. Phys. Commun. **272**, 108246 (2022).
[33] J. C. Meng and T. Colonius, Numerical simulation of the aerobreakup of a water droplet, J. Fluid Mech. **835**, 1108 (2018).
[34] P. Das and H. S. Udaykumar, A sharp-interface method for the simulation of shock-induced vaporization of droplets, J. Comput. Phys. **405**, 109005 (2020).
[35] H. J. Q. Wan, R. Deiterding, and V. Eliasson, Numerical and experimental investigation of oblique shock wave reflection off a water wedge, J. Fluid Mech. **826**, 732 (2017).
[36] K. Schmidmayer and L. Biasiori-Poulanges, Geometry effects on the droplet shock-induced cavitation, Phys. Fluids **35**, 063315 (2023).
[37] B. Dorschner, L. Biasiori-Poulanges, K. Schmidmayer, H. El-Rabii, and T. Colonius, On the formation and recurrent shedding of ligaments in droplet aerobreakup, J. Fluid Mech. **904**, A20 (2020).
[38] R. W. Forehand, K. C. Nguyen, C. J. Anderson, R. Shannon, S. M. Grace, and M. P. Kinzel, A numerical assessment of shock–droplet interaction modeling including cavitation, Phys. Fluids **35**, 023315 (2023).
[39] B. Guan, Y. Liu, C. Y. Wen, and H. Shen, Numerical study on liquid droplet internal flow under shock impact, AIAA J. **56**, 3382 (2018).
[40] Z. Wang, T. Hopfes, M. Giglmaier, and N. A. Adams, Effect of Mach number on droplet aerobreakup in shear stripping regime, Exp. Fluids **61**, 193 (2020).
[41] R. Abgrall, How to prevent pressure oscillations in multicomponent flow calculations: A quasi conservative approach, J. Comput. Phys. **125**, 150 (1996).
[42] D. Banuti, M. Raju, P. C. Ma, M. Ihme, and J.-P. Hickey, Seven questions about supercritical fluids towards a new fluid state diagram, in *Proceedings of the 55th AIAA Aerospace Sciences Meeting* (AIAA, Reston, VA, 2017), p. 1106.
[43] M. Raju, D. T. Banuti, P. C. Ma, and M. Ihme, Widom lines in binary mixtures of supercritical fluids, Sci. Rep. **7**, 3027 (2017).
[44] C. F. Delale, *Bubble Dynamics and Shock Waves* (Springer, Berlin, 2013).
[45] T. Theofanous, Aerobreakup of Newtonian and viscoelastic liquids, Annu. Rev. Fluid Mech. **43**, 661 (2011).
[46] N. J. Zabusky, Vortex paradigm for accelerated inhomogeneous flows: Visiometrics for the Rayleigh-Taylor and Richtmyer-Meshkov environments, Annu. Rev. Fluid Mech. **31**, 495 (1999).
[47] V. Duke-Walker, W. C. Maxon, S. R. Almuhna, and J. A. McFarland, Evaporation and breakup effects in the shock-driven multiphase instability, J. Fluid Mech. **908**, A13 (2021).
[48] J. W. J. Kaiser, J. M. Winter, S. Adami, and N. A. Adams, Investigation of interface deformation dynamics during high-Weber number cylindrical droplet breakup, Int. J. Multiphase Flow **132**, 103409 (2020).
[49] S. Sharma, A. P. Singh, S. S. Rao, A. Kumar, and S. Basu, Shock induced aerobreakup of a droplet, J. Fluid Mech. **929**, A27 (2021).
[50] P. Tudisco and S. Menon, Numerical investigations of phase-separation during multi-component mixing at super-critical conditions, Flow Turbul. Combust. **104**, 693 (2020).
[51] B. Boyd and D. Jarrahbashi, A diffuse-interface method for reducing spurious pressure oscillations in multicomponent transcritical flow simulations, Comput. Fluids **222**, 104924 (2021).

[52] B. Boyd and D. Jarrahbashi, Numerical study of the transcritical shock-droplet interaction, Phys. Rev. Fluids **6**, 113601 (2021).
[53] S. Wang, Z. Jiao, X. Huang, C. Yang, and N. Nguyen, Acoustically induced bubbles in a microfluidic channel for mixing enhancement, Microfluid. Nanofluid. **6**, 847 (2009).
[54] O. Shpak, M. Verweij, N. de Jong, and M. Versluis, Droplets, bubbles and ultrasound interactions, Ther. Ultrasound **880**, 157 (2016).
[55] L. Ming, N. Zhi, and S. Chunhua, Numerical simulation of cavitation bubble collapse within a droplet, Comput. Fluids **152**, 157 (2017).
[56] G. Wang, Y. Wang, D. Li, and B. Guan, Numerical study on shock-accelerated gas rings, Phys. Fluids **32**, 026102 (2020).
[57] L. Feng, J. Xu, Z. Zhai, and X. Luo, Evolution of shock-accelerated double-layer gas cylinder, Phys. Fluids **33**, 086105 (2021).
[58] Y. Liang, Y. Jiang, C. Wen, and Y. Liu, Interaction of a planar shock wave and a water droplet embedded with a vapour cavity, J. Fluid Mech. **885**, R6 (2020).
[59] G. Xiang and B. Wang, Numerical study of a planar shock interacting with a cylindrical water column embedded with an air cavity, J. Fluid Mech. **825** 825 (2017).
[60] K. Yang and T. Aoki, Weakly compressible Navier-Stokes solver based on evolving pressure projection method for two-phase flow simulations, J. Comput. Phys. **431**, 110113 (2021).
[61] T. Schmitt, L. Selle, A. Ruiz, and B. Cuenot, Large-eddy simulation of supercritical-pressure round jets, AIAA J. **48**, 2133 (2010).
[62] H. Terashima and M. Koshi, Approach for simulating gas-liquid-like flows under supercritical pressures using a high-order central differencing scheme, J. Comput. Phys. **231**, 6907 (2012).
[63] G. Lacaze, T. Schmitt, A. Ruiz, and J. C. Oefelein, Comparison of energy-, pressure- and enthalpy-based approaches for modeling supercritical flows, Comput. Fluids **181**, 35 (2019).
[64] K. Kitamura and E. Shima, Pressure-equation-based SLAU2 for oscillation-free, supercritical flow simulations, Comput. Fluids **163**, 86 (2018).
[65] H. Terashima and M. Koshi, Strategy for simulating supercritical cryogenic jets using high-order schemes, Comput. Fluids **85**, 39 (2013).
[66] R. Abgrall and S. Karni, Computations of compressible multifluids, J. Comput. Phys. **169**, 594 (2001).
[67] C. P. Egerer, S. J. Schmidt, S. Hickel, and N. A. Adams, Efficient implicit LES method for the simulation of turbulent cavitating flows, J. Comput. Phys. **316**, 453 (2016).
[68] S. J. Schmidt, A low Mach number consistent compressible approach for simulation of cavitating flow, Ph.D. thesis, Technical University of Munich, 2015.
[69] Y. Jiao, S. J. Schmidt, and N. A. Adams, An all-Mach consistent numerical scheme for simulation of compressible multi-component fluids including surface tension, cavitation, turbulence modeling and interface sharpening on compact stencils, Comput. Fluids **274**, 106186 (2024).
[70] T. Trummler, S. J. Schmidt, and N. A. Adams, Investigation of condensation shocks and re-entrant jet dynamics in a cavitating nozzle flow by Large-Eddy Simulation, Int. J. Multiphase Flow **125**, 103215 (2020).
[71] E. Knudsen, E. M. Doran, V. Mittal, J. Meng, and W. Spurlock, Compressible Eulerian needle-to-target large eddy simulations of a diesel fuel injector, Proc. Combust. Inst. **36**, 2459 (2017).
[72] J. Matheis and S. Hickel, Multi-component vapor-liquid equilibrium model for LES of high-pressure fuel injection and application to ECN Spray A, Int. J. Multiphase Flow **99**, 294 (2018).
[73] A. M. Ruiz, G. Lacaze, J. C. Oefelein, R. Mari, B. Cuenot, L. Selle, and T. Poinsot, Numerical benchmark for high-Reynolds-number supercritical flows with large density gradients, AIAA J. **54**, 1445 (2016).
[74] H. Müller, C. A. Niedermeier, J. Matheis, M. Pfitzner, and S. Hickel, Large-eddy simulation of nitrogen injection at trans- and supercritical conditions, Phys. Fluids **28**, 015102 (2016).
[75] W. Wei, H. Liu, M. Xie, M. Jia, and M. Yue, Large eddy simulation and proper orthogonal decomposition analysis of fuel injection under trans/supercritical conditions, Comput. Fluids **179**, 150 (2019).
[76] N. Okong'o and J. Bellan, Perturbation and initial Reynolds number effects on transition attainment of supercritical, binary, temporal mixing layers, Comput. Fluids **33**, 1023 (2004).

[77] D.-Y. Peng and D. B. Robinson, A new two-constant equation of state, Ind. Eng. Chem. Fundam. **15**, 59 (1976).
[78] B. J. McBride, *Coefficients for Calculating Thermodynamic and Transport Properties of Individual Species* (NASA, Office of Management, Scientific and Technical Information Program, Washington, DC, 1993), Vol. 4513.
[79] G. Billet and R. Abgrall, An adaptive shock-capturing algorithm for solving unsteady reactive flows, Comput. Fluids **32**, 1473 (2003).
[80] G. Billet and J. Ryan, A Runge-Kutta discontinuous Galerkin approach to solve reactive flows: The hyperbolic operator, J. Comput. Phys. **230**, 1064 (2011).
[81] Y. Lv and M. Ihme, Discontinuous Galerkin method for multi-component chemically reacting flows and combustion, J. Comput. Phys. **270**, 105 (2014).
[82] P. C. Ma, H. Wu, D. T. Banuti, and M. Ihme, On the numerical behavior of diffuse-interface methods for transcritical real-fluids simulations, Int. J. Multiphase Flow **113**, 231 (2019).
[83] S. Kawai, H. Terashima, and H. Negishi, A robust and accurate numerical method for transcritical turbulent flows at supercritical pressure with an arbitrary equation of state, J. Comput. Phys. **300**, 116 (2015).
[84] P. C. Ma, H. Wu, T. Jaravel, L. Bravo, and M. Ihme, Large-eddy simulations of transcritical injection and auto-ignition using diffuse-interface method and finite-rate chemistry, Proc. Combust. Inst. **37**, 3303 (2019).
[85] C. Traxinger, M. Pfitzner, S. Baab, G. Lamanna, and B. Weigand, Experimental and numerical investigation of phase separation due to multicomponent mixing at high-pressure conditions, Phys. Rev. Fluids **4**, 074303 (2019).
[86] D. T. Banuti, P. C. Ma, and M. Ihme, Phase separation analysis in supercritical injection using large-eddy-simulation and vapor-liquid-equilibrium, in *Proceedings of the 53rd AIAA/SAE/ASEE Joint Propulsion Conference* (AIAA, Reston, VA, 2017), p. 4764.
[87] A. Baeza, R. Bürger, P. Mulet, and D. Zorío, An efficient third-order WENO scheme with unconditionally optimal accuracy, SIAM J. Sci. Comput. **42**, A1028 (2020).
[88] E. F. Toro, *Riemann Solvers and Numerical Methods for Fluid Dynamics: A Practical Introduction*, 3rd ed., (Springer, Dordrecht, 2009).
[89] J. W. Jacobs, The dynamics of shock accelerated light and heavy gas cylinders, Phys. Fluids A **5**, 2239 (1993).
[90] Z. Zhai, T. Si, L. Zou, and X. Luo, Jet formation in shock-heavy gas bubble interaction, Acta Mech. Sin. **29**, 24 (2013).
[91] L. Zou, Z. Zhai, J. Liu, Y. Wang, and C. Liu, Energy convergence effect and jet phenomenon of shock-heavy spherical bubble interaction, Sci. China: Phys., Mech. Astron. **58**, 014711 (2015).
[92] E. Fan, B. Guan, C.-Y. Wen, and H. Shen, Numerical study on the jet formation of simple-geometry heavy gas inhomogeneities, Phys. Fluids **31**, 026103 (2019).
[93] B. Guan, H. Yang, H. Yang, and G. Wang, On the irregular jet formation of shock-accelerated spherical heavy gas bubbles, Phys. Fluids **34**, 126111 (2022).
[94] A. M. Abd-el Fattah and L. F. Henderson, Shock waves at a slow-fast gas interface, J. Fluid Mech. **89**, 79 (1978).
[95] See Supplemental Material at http://link.aps.org/supplemental/10.1103/PhysRevFluids.9.074002 for the evolution of surface deformation with different isosurface values.
[96] T. G. Theofanous and G. J. Li, On the physics of aerobreakup, Phys. Fluids **20**, 052103 (2008).
[97] N. Liu, Z. Wang, M. Sun, H. Wang, and B. Wang, Numerical simulation of liquid droplet breakup in supersonic flows, Acta Astronaut. **145**, 116 (2018).
[98] T. G. Theofanous, V. V. Mitkin, C. L. Ng, C. H. Chang, X. Deng, and S. Sushchikh, The physics of aerobreakup. II, Viscous liquids, Phys. Fluids **24**, 022104 (2012).
[99] S. Sharma, A. P. Singh, and S. Basu, On the dynamics of vortex-droplet co-axial interaction: Insights into droplet and vortex dynamics, J. Fluid Mech. **918**, A37 (2021).
[100] A. Zandian, W. A. Sirignano, and F. Hussain, Planar liquid jet: Early deformation and atomization cascades, Phys. Fluids **29**, 062109 (2017).

[101] A. Zandian, W. A. Sirignano, and F. Hussain, Vorticity dynamics in a spatially developing liquid jet inside a co-flowing gas, J. Fluid Mech. **877**, 429 (2019).
[102] D. Jarrahbashi, W. A. Sirignano, P. P. Popov, and F. Hussain, Early spray development at high gas density: Hole, ligament and bridge formations, J. Fluid Mech. **792**, 186 (2016).
[103] A. Zandian, W. A. Sirignano, and F. Hussain, Length-scale cascade and spread rate of atomizing planar liquid jets, Int. J. Multiphase Flow **113**, 117 (2019).
[104] K. G. Harstad, R. S. Miller, and J. Bellan, Efficient high-pressure state equations, AlChE J. **43**, 1605 (1997).
[105] J. H. Perry, *Chemical Engineers' Handbook* (ACS Publications, Washington, DC, 1950).
[106] G. Wilczek-Vera and J. H. Vera, Understanding cubic equations of state: A search for the hidden clues of their success, AlChE J. **61**, 2824 (2015).
[107] P. Yi, S. Yang, C. Habchi, and R. Lugo, A multicomponent real-fluid fully compressible four-equation model for two-phase flow with phase change, Phys. Fluids **31**, 026102 (2019).
[108] R. P. Fedkiw, T. Aslam, B. Merriman, and S. Osher, A non-oscillatory Eulerian approach to interfaces in multimaterial flows (the ghost fluid method), J. Comput. Phys. **152**, 457 (1999).
[109] A. Bagabir and D. Drikakis, Mach number effects on shock-bubble interaction, Shock Waves **11**, 209 (2001).